Rotational waves generated by current-topography interaction

By Marcelo V. Flamarion[*]*, Paul A. Milewski*[†] *and André Nachbin*[‡]*,*

Dedicated to Roger Grimshaw

We study nonlinear free-surface rotational waves generated through the interaction of a vertically sheared current with a topography. Equivalently, the waves may be generated by a pressure distribution along the free surface. A forced Korteweg-de Vries equation (fKdV) is deduced incorporating these features. The weakly nonlinear, weakly dispersive reduced model is valid for small amplitude topographies. In order to study the effect of gradually increasing the topography amplitude, the free surface Euler equations are formulated in the presence of a variable depth and a sheared current of constant vorticity. Under constant vorticity, the harmonic velocity component is formulated in a simplified canonical domain, through the use of a conformal mapping which flattens both the free surface as well as the bottom topography. Critical, supercritical and subcritical Froude number regimes are considered, while the bottom amplitude is gradually increased in both the irrotational and rotational wave regimes. Solutions to the fKdV model are compared to those from the Euler equations. We show that for rotational waves the critical Froude number is shifted away from 1. New stationary solutions are found and their stability tested numerically.

1 Introduction

Water waves is a research area in Fluid Dynamics and Partial Differential Equations which is of great current interest due to the large number of problems it spawns from theory to computations, and with many practical applications. Reduced modeling is a topic which permits simplifying the problem in a systematic fashion, enabling theoretical results and more efficient computations. The Korteweg-de Vries (KdV) equation is an example of such reduced model applicable to long surface waves when the water is shallow compared to horizontal length scales of motion. Roger Grimshaw has made many scientific contributions in this field and with admiration we dedicate this work to his 80th birthday.

[*]Address for correspondence: Marcelo V. Flamarion, Unidade Acadêmica do Cabo de Santo Agostinho, Universidade Federal Rural de Pernambuco, BR 101 Sul, 5225, Ponte dos Carvalhos, Cabo de Santo Agostinho, Pernambuco, PE, Brazil, CEP 54503-900; e-mail: marcelo.flamarion@ufrpe.br

[†]Address for correspondence: Paul A. Milewski, Department of Mathematics, University of Bath, Claverton Down, Bath BA2 7AY; e-mail: P.A.Milewski@bath.ac.uk

[‡]Address for correspondence: André Nachbin, IMPA, Estrada Dona Castorina 110, Jardim Botânico, Rio de Janeiro, RJ, Brazil, CEP 22460-320; e-mail: nachbin@impa.br

1.1 Motivation

In the present article we study nonlinear surface waves generated due to a constant vorticity flow over a submarine obstacle on the bottom of a channel or due to a localised pressure distribution along the free surface. Through a choice of the Froude number, we position ourselves in the nearly resonant regime. We consider solutions of both the forced KdV equation as well as the full Euler equations. The constant vorticity assumption results in a linear shear flow away from the forcing and when there are no waves. As soon as the waves or the topography are sufficiently large, the flow ceases to look like a linear horizontal shear and adjusts accordingly. In other words, while the upstream flow has a linear profile, this is not the case everywhere, as the presence of a wave and of the topography alters the flow substantially in order to achieve a constant vorticity velocity field solving the full Euler equations and boundary conditions.

Nonlinear surface waves with constant vorticity are a problem of interest in applications and in applied analysis. The paper by Teles and Peregrine [1] conjectured flow features which were later investigated by both numerical and theoretical researchers. These include numerical studies with traveling waves, such as that by Vasan and Oliveras [2] as well as by Ribeiro-Jr et al. [3]. Applied analysis researchers recently made efforts in understanding the impact of constant vorticity on nonlinear traveling wave solutions. A good source of recent articles is found in the theme volume edited by Constantin [4]. Constant vorticity has an impact, for example, on the formation of a critical layer beneath traveling waves [5]. This critical layer has a Kelvin cat eye structure together with the respective formation of critical points, as numerically illustrated by the authors in [3].

In the present manuscript we consider a more general setting where rotational waves are spontaneously generated by the topography or a pressure distribution, and not imposed by special traveling wave initial data. The choice of constant vorticity still allows for a decomposition of the flow to be applied, in which the principal component is harmonic. This decomposition is not possible in more general settings. While more general vorticity distributions may be more realistic, the respective mathematical modeling, as well as theoretical access, are much harder than in the constant vorticity case. In his introduction, Constantin [4] calls attention that "constant vorticity is representative when the waves are long compared with the water depth since in this case it is the existence of a non-zero mean vorticity that is important rather than its specific distribution. In the present study we consider the long wave (weakly dispersive) regime.

It is important to call attention that our study regards the impact of constant vorticity in the nearly resonant wave generation regime. Namely, we consider Froude numbers near its critical value which no longer corresponds to $U_0/\sqrt{gh_0} \approx 1$, as is the case for irrotational currents of strength U_0 in a fluid layer of depth h_0.

1.2 Background

The main parameter in the study is therefore the Froude number $F = U_0/(gh_0)^{1/2}$, together with the spatial characteristics of either the bottom topography or the pressure distribution. Their amplitudes and length-scale play an important role. We denote by U_0 the speed of the bottom obstacle or of the moving pressure distribution in a frame where the velocity induced by the background shear is zero. We can also consider U_0 to be the characteristic speed of the underlying current when these bottom and pressure disturbances are taken to be stationary. The channel's reference depth is h_0 and the acceleration due to gravity denoted by g. The water surface is initially taken at rest. Our main goal is to investigate the dynamical features of nonlinear waves generated by the interaction of the current

with the topographic or pressure forcing.

From the Applied Mathematics point of view, our investigation considers reduced modeling, where we first deduce a forced Korteweg-de Vries equation (fKdV) which combines the effects of a sheared current interacting with a topography, or equivalently a pressure distribution. We also present a more complete Euler equation formulation using conformal mapping, having in mind that we want to explore this wave generation problem beyond the fKdV regime. The Euler equations are presented in the canonical (conformally mapped) domain. The computational domain becomes a uniform flat strip, more amenable to computations. A similar conformal mapping formulation has been used by Viotti et al. [25, 26], but their underlying current is irrotational. In Viotti et al. [25] two examples are considered. First an initial disturbance is provided to study the solitary wave fission over a submerged step. And finally an example with one supercritical stationary wave generation, due to the presence of a submerged triangular obstacle. In Viotti and Dias [26] an initial random wave field is given and allowed to propagate towards a long shallower region, allowing for extreme wave formation. The scope of these interesting studies is different from ours.

Several aspects of this surface wave-generation problem have been studied by many researchers. Akylas [27] deduced an fKdV equation for a pressure distribution moving with constant speed along the free surface. Akylas showed that for $F \neq 1$ the linearized Euler equations produce solutions given by a stationary wave, where transients are outgoing as $t \to \infty$. Nevertheless for the critical (resonant) regime $F = 1$ the linear model predicts that the wave amplitude grows indefinitely in time. Grimshaw and Smyth [23] considered this wave generation problem due to the interaction of a uniform (constant) current with a submerged topography, in the form of a Gaussian mound. They obtained approximate analytical solutions which were well compared with numerical solutions. Near the critical regime, they observed waves propagating both downstream as well as upstream. The sign of the forcing was important. For a positive forcing a series of solitary waves propagate upstream. Downstream one usually observes an oscillatory wavetrain for subcritical forcing. This was actually first observed numerically by Wu and Wu [29]. Wu [28] studied the mechanism for the upstream generation of solitary waves. Camassa and Wu [20, 21] studied numerically, with the fKdV, the stability of stationary solitary waves. Chardard et al. [9] studied numerically, with the fKdV, the stability of solitary waves for multiple submerged obstacles.

More recently Albalwi, Marchant and Smyth [16] deduced a higher-order fKdV model, up to fifth-order, which they called the (extended) eKdV model. They studied the nearly critical regime for a constant current interacting with a submerged topography. They compare their model with that of Grimshaw and Smyth [23]. In particular, they show that the eKdV's higher order terms capture the onset of wave breaking, in the form of an undular bore. Before wave breaking, they comment on the envelope of the downstream oscillatory wavetrain. For the eKdV solution the envelope is shaper, decaying faster than that of the respective fKdV model. This is also observed in the present work.

With the Euler equations and a boundary integral method, Vanden-Broeck and Tuck [13] studied stationary subcritical waves generated by a moving pressure distribution and their connection with ship generated waves. Later Asavanant et al. [11] studied this problem in both the subcritical and supercritical regimes, also with boundary integrals. They explored different parameter regimes, including effects of pressure intensity and distribution length. Binder, Vanden-Broeck and Dias [8] used the boundary integral method to compute stationary supercritical solutions in the presence of two triangles along the bottom.

Comparing the fKdV model with the Euler equations, is the spirit of the present work and, the inclusion of shear, has been adressed by some authors. Grimshaw and Maleewong [22] used the fKdV model to benchmark a boundary integral method for the Euler equations. They considered a transcritical

regime with a small amplitude pressure forcing. Choi and Camassa [31] used the conformal mapping technique, introduced by Dyachenko et al. [6], to flatten the free surface elevation in the canonical complex plane and compare solitary waves produced by both models.

Other studies have considered solitary waves using the Euler equations with a conformal mapping technique, as for example some mentioned above [25, 26]. Choi [30] studied travelling waves with the Euler equations in the presence of a sheared current of constant vorticity. The bottom was considered flat. Milewski et al. [18] also used the (free surface) conformal mapping technique to study collisions of gravity-capillary solitary waves. Nachbin [7], on the other hand, used conformal mapping to flatten the bottom topography for weakly nonlinear waves in the absence of a current. Here both ingredients are combined for rotational waves, namely flattening both the free surface and the bottom topography.

Finally we should mention about related work on internal waves. Internal waves are not within the scope of our study, but their interaction and generation by isolated topography have similarities with the study here presented. For the interested reader a partial list of references follow. A comprehensive review of linear internal wave interaction with topography, can be found in the 1995 book by Baines [33]. Grimshaw and Yi [34] studied stratified flows forced resonantly by topography and a forced KdV equation is deduced. Wang and Redekopp [32] studied long internal waves in shear flows in the regime of topographic resonance. They were interested in the internal wave-bottom interaction, and its passage-through-resonance enhancing resuspension of nutrients from the boundary layer region. They considered two layers of different densities and different constant vorticity, and their reduced modeling led to a forced KdV equation which is solved numerically. As expected, their forced KdV equation for internal waves emits solitary waves upstream, similar to what is seen here with both the fKdV and Euler models.

Helfrich and Melville [35] in their 2006 review article report on long nonlinear internal solitary-like waves, commonly observed in coastal dynamics. An overview is presented primarily from the point of view of the Korteweg-de Vries equation. Internal wave generation by topography is discussed in section 3.1. The KdV transcritical regime is depicted in figure 6, with wave profiles similar to those depicted in the present work. Helfrich and Melville [35] call attention that observations often display waves beyond the weakly nonlinear KdV regime and add that properties of these waves should be explained with fully nonlinear models.

In a more recent review, Lamb [36] reports on internal wave breaking in the continental shelf. While theoretical, numerical and laboratory studies mostly focus on simple geometries, Lamb calls for more detailed modeling since ocean scenarios reveal much more complex geometries and fluid motions.

Soontiens et al. [37] studied trapped internal waves over isolated topography in the presence of a background shear. Continuous stratification is considered together with the Boussinesq approximation. This configuration had been used earlier by Stastna and Peltier [38] for the resonant generation of solitary-like waves. They compared two classes of approximate models, one class being weakly nonlinear while the other (fully nonlinear) connected to the conjugate flow theory, is based on a simpler ordinary differential equation (ODE) eigenvalue problem [38, 37]. The (trapped) steady waves studied are in the supercritical regime. Soontiens et al. [37] do not specify a functional form for the topography nor for the background current, and therefore derive a general version of the Dubreill-Jacotin-Long equation, which is a nonlinear elliptic (time independent) equation formulated in terms of the isopycnal displacement. One of their goals was to compute internal waves with closed streamlines, also called vortex cores. Without reference to the respective critical points, these are submarine structures similar to the critical layers for traveling rotational (surface) waves over a flat bottom [3, 5], mentioned above in section 1.1. A Dubreil-Jacotin equation has been used in the analysis of surface waves with vorticity, based on a hodograph transformation using the stream-function [5, 39]. However the Dubreil-Jacotin formulation

is not well suited for capturing the precise location of the critical (stagnation) points, in the particle's phase portrait representation, because it has singularities at these critical points. Our alternative for accurately finding the critical points, of the closed streamlines [3], was a conformal mapping similar to the one here presented.

This article is organized as follows. In section 2 we deduce the fKdV equation which combines topographic and pressure forcing with a sheared (constant vorticity) current. In section 3 we formulate the potential theory equations in the (conformally mapped) canonical domain. In section 4 we have the numerical methods and numerical results. The conclusions are given in section 5, and a resolution study for the Euler equations is presented in the appendix.

2 Forced Kortweg-de Vries equation for rotational waves

We consider the two-dimensional incompressible flow of an inviscid fluid of density ρ. In this section we deduce a long-wave equation for free surface waves generated by the interaction of both a surface pressure distribution and a topography with an underlying depth-varying current. The deduced forced Kortweg-de Vries (fKdV) model will account for the generation and propagation of rotational waves.

We begin with the free-surface Euler equations [10]. Let the free surface be denoted by $\zeta(x,t)$ and the bottom topography by $h(x)$. We have that

$$\begin{aligned}
&u_t + uu_x + vu_y = -\frac{p_x}{\rho}, \quad \text{for} \quad h(x) < y < \zeta(x,t),\\
&v_t + uv_x + vv_y = -\frac{p_y}{\rho} - g, \quad \text{for} \quad h(x) < y < \zeta(x,t),\\
&u_x + v_y = 0, \quad \text{for} \quad h(x) < y < \zeta(x,t),\\
&p = P(x), \quad \text{at} \quad y = \zeta(x,t),\\
&v = \zeta_t + u\zeta_x, \quad \text{at} \quad y = \zeta(x,t),\\
&v = uh_x, \quad \text{at} \quad y = h(x).
\end{aligned} \tag{1}$$

We have denoted the fluid velocity by (u,v), the gravity acceleration by g, the surface pressure distribution by P, while the pressure in the fluid bulk by p. We consider all functions (u, v, ζ, h and p) in equations (1) to be smooth and decaying to zero as $|x| \to \infty$. Consider the following set of dimensionless variables, where λ is a reference wavelength, a a reference amplitude, h_0 a reference depth and $\lambda/\sqrt{gh_0}$ a reference time-scale:

$$\begin{aligned}
&x \to \lambda x, \quad y \to h_0 y, \quad t \to \frac{\lambda}{\sqrt{gh_0}} t,\\
&u \to \sqrt{gh_0}\, u, \quad v \to \frac{h_0\sqrt{gh_0}}{\lambda} v, \quad h \to h_0 h.
\end{aligned}$$

We also have that

$$p \to \rho g h_0 (h_0 - y) + \rho g h_0 p, \quad P \to \rho g h_0 P \quad \text{and} \quad \zeta \to h_0 + a\zeta.$$

Introducing the dispersion parameter $\mu = h_0/\lambda$ and the nonlinearity parameter $\epsilon = a/h_0$, the dimen-

sionless form of equations (1) is given as:

$$\begin{aligned}
&u_t + uu_x + vu_y = -p_x, \quad \text{for} \quad h(x) < y < 1 + \epsilon\zeta(x,t),\\
&\mu^2\{v_t + \epsilon(uv_x + vv_y)\} = -p_y, \quad \text{for} \quad h(x) < y < 1 + \epsilon\zeta(x,t),\\
&u_x + v_y = 0, \quad \text{for} \quad h(x) < y < 1 + \epsilon\zeta(x,t),\\
&p = P + \epsilon\zeta, \quad \text{at} \quad y = 1 + \epsilon\zeta(x,t),\\
&v = \epsilon(\zeta_t + u\zeta_x), \quad \text{at} \quad y = 1 + \epsilon\zeta(x,t),\\
&v = uh_x, \quad \text{at} \quad y = h(x).
\end{aligned} \tag{2}$$

In order to accommodate the perturbative effects of both the pressure and the topography, we rescale in the form:

$$u \to U(y) + \epsilon u, \quad v \to \epsilon v, \quad p \to \epsilon p, \quad P \to \epsilon^2 P \ \text{ e } \ h \to \epsilon^2 h. \tag{3}$$

The depth-dependent imposed current $U(y)$ is therefore the dominant horizontal speed component. We will see below that in this scaling limit $U(y)$ is not arbitrary. Using the typical balance for a KdV model, $\mu^2 = \epsilon$, and substituting (3) in (2) yields

$$\begin{aligned}
&u_t + U(y)u_x + U'(y)v + \epsilon(uu_x + vu_y) = -p_x, \quad \text{for} \quad h(x) < y < 1 + \epsilon\zeta(x,t),\\
&\epsilon\{v_t + U(y)v_x + \epsilon(uv_x + vv_y)\} = -p_y, \quad \text{for} \quad h(x) < y < 1 + \epsilon\zeta(x,t),\\
&u_x + v_y = 0, \quad \text{for} \quad h(x) < y < 1 + \epsilon\zeta(x,t),\\
&p = \zeta + \epsilon P, \quad \text{at} \quad y = 1 + \epsilon\zeta,\\
&v = \zeta_t + U(y)\zeta_x + \epsilon u\zeta_x, \quad \text{at} \quad y = 1 + \epsilon\zeta,\\
&v = \epsilon h_x U(y) + \epsilon^2 h_x u, \quad \text{at} \quad y = \epsilon^2 h.
\end{aligned}$$

We introduce a traveling coordinate $\xi = x - ct$, where c is yet to be determined, and the slowly varying time $\tau = \epsilon t$. In this frame we have that

$$\begin{aligned}
&(U(y) - c)u_\xi + U'(y)v + \epsilon(u_\tau + uu_\xi + vu_y) = -p_\xi, \quad \text{for} \quad h < y < 1 + \epsilon\zeta,\\
&\epsilon\{(U(y) - c)v_\xi + \epsilon(v_\tau + uv_\xi + vv_y)\} = -p_y, \quad \text{for} \quad h < y < 1 + \epsilon\zeta,\\
&u_\xi + v_y = 0, \quad \text{for} \quad h < y < 1 + \epsilon\zeta,\\
&p = \zeta + \epsilon P, \quad \text{at} \quad y = 1 + \epsilon\zeta,\\
&v = (U(y) - c)\zeta_\xi + \epsilon(\zeta_\tau + u\zeta_\xi), \quad \text{at} \quad y = 1 + \epsilon\zeta,\\
&v = \epsilon h_\xi U(y) + \epsilon^2 h_\xi u, \quad \text{at} \quad y = \epsilon^2 h.
\end{aligned} \tag{4}$$

For a weakly nonlinear regime, consider a power series expansion in terms of the small parameter ϵ. In the absence of forcing (pressure and topography) Freeman and Johnson [17] studied rotational solitary waves, with expansions in the form

$$q(\xi, y, \tau; \epsilon) = \sum_{n=0}^{\infty} \epsilon^n q_n(\xi, y, \tau), \quad \zeta(\xi, \tau) = \sum_{n=0}^{\infty} \epsilon^n \zeta_n(\xi, \tau), \tag{5}$$

where $q = u, v, p$. Substituting (5) in (4) one obtains a family of problems, in an $\mathcal{O}(\epsilon^n)$-hierarchy. The $\mathcal{O}(\epsilon^0)$-equations are:

$$\begin{aligned}
&(U(y) - c)u_{0\xi} + U'(y)v_0 = -p_{0\xi}, \quad p_{0y} = 0, \quad u_{0\xi} + v_{0y} = 0, \quad \text{for} \quad 0 < y < 1,\\
&p_0 = \zeta_0, \quad v_0 = (U(y) - c)\zeta_{0\xi}, \quad \text{at} \quad y = 1 \ \text{ and } \ v_0 = 0, \quad \text{at} \quad y = 0.
\end{aligned} \tag{6}$$

By integration one obtains the solution

$$v_0 = \left\{ (U(y)-c) \int_0^y \frac{dz}{(U(y)-c)^2} \right\} \zeta_{0\xi}, \tag{7}$$

$$u_0 = -\left\{ \frac{1}{U(y)-c} + U'(y) \int_0^y \frac{dz}{(U(y)-c)^2} \right\} \zeta_0. \tag{8}$$

Substituting (7) in the kinematic condition in (6), yields the compatibility condition known as Burns condition:

$$\int_0^1 \frac{1}{(U(y)-c)^2} dy = 1, \tag{9}$$

from which the speed c can be computed later. Burns condition is discussed in detail in the book by Johnson [40], pages 255-262. This condition is obtained from the underlying linear problem. For a uniform current, the linear solution does not exist if $U(y_c) = c$, at some critical depth y_c. However this *critical depth* condition is not satisfied for a linear shear [40]. The first order approximation ζ_0, for the free surface elevation, will be defined at the next set of equations. At $\mathcal{O}(\epsilon^1)$ we have that:

$$\begin{aligned}
&(U(y)-c)u_{1\xi} + U'(y)v_1 + u_{0\tau} + u_0 u_{0\xi} + v_0 u_{0y} = -p_{1\xi}, \quad \text{for} \quad 0 < y < 1, \\
&(U(y)-c)v_{0\xi} = -p_{1y}, \quad \text{for} \quad 0 < y < 1, \\
&u_{1\xi} + v_{1y} = 0, \quad \text{for} \quad 0 < y < 1, \\
&p_{1y} = \zeta_1 + P, \quad \text{at} \quad y = 1, \\
&v_1 + \zeta_0 v_{0y} = (U(y)-c)\zeta_{1\xi} + U'(y)\zeta_0\zeta_{0\xi} + \zeta_{0\tau} + u_0\zeta_{0\xi}, \quad \text{at} \quad y = 1, \\
&v = U(y)h_\xi, \quad \text{at} \quad y = 0.
\end{aligned} \tag{10}$$

The kinematic condition in (4) has been Taylor-expanded about $y = 1$. From equations (6) and (10) one arrives at:

$$p_1 = \zeta_1 + P + \left\{ \int_y^1 (U(y)-c)^2 I_2(y) dy \right\} \zeta_{0\xi\xi}, \tag{11}$$

$$\begin{aligned}
&(U(y)-c)^2 \left\{ \frac{v_1}{U(y)-c} \right\}_y + \left\{ \frac{1}{U(y)-c} + U'(y)I_2(y) \right\} \zeta_{0\tau} \\
&- \left\{ \frac{1}{U(y)-c} + U'(y)I_2(y) \right\}^2 \zeta_0\zeta_{0\xi} = \zeta_{1\xi} + P_\xi + \left(\int_y^1 (U(y)-c)^2 I_2(y) dy \right) \zeta_{0\xi\xi\xi},
\end{aligned} \tag{12}$$

where

$$I_n(y) \equiv \int_0^y \frac{dy}{(U(y)-c)^n}, \quad \text{for} \quad n = 1, 2, 3, 4.$$

Integrate equation (12) from 0 to y, together with the bottom condition $v_1 = U(y)h_\xi$, at $y = 0$. We have that

$$\begin{aligned}
v_1 = (U(y)-c) \Bigg\{ &\left(\frac{I_2(y)}{U(y)-c} - 2I_3(y) \right) \zeta_{0\tau} \\
&+ \left(I_4(y) + 4 \int_0^y \frac{U'(y)I_2(y)}{(U(y)-c)^3} dy - \frac{U'(y)I_2(y)}{U(y)-c} \right) \zeta_0\zeta_{0\xi} + I_2(y)\zeta_{1\xi} + I_2(y)P_\xi \\
&+ \zeta_{0\xi\xi\xi} \int_0^y \frac{1}{(U(y)-c)^2} \left[\int_y^1 (U(y)-c)^2 I_2(y) dy \right] dy \Bigg\} + \frac{U(y)-c}{U(0)-c} U(0) h_\xi.
\end{aligned}$$

Evaluating at $y=1$, and imposing the kinematic condition in (10), yields

$$\begin{aligned}(U(1)-c)\zeta_{1\xi}+U'(1)\zeta_0\zeta_{0\xi}+\zeta_{0\tau}-2\left\{\frac{1}{U(1)-c}+U'(1)I_2(1)\right\}\zeta_0\zeta_{0\xi}\\ +\frac{U(1)-c}{U(0)-c}U(0)h_\xi=(U(1)-c)\left\{\left(\frac{I_2(1)}{U(1)-c}-2I_3(1)\right)\zeta_{0\tau}\right.\\ \left.+\left(I_4(1)+4\int_0^1\frac{U'(y)I_2(y)dy}{(U(y)-c)^3}-\frac{U'(1)I_2(1)}{U(1)-c}\right)\zeta_0\zeta_{0\xi}+I_2(1)\zeta_{1\xi}+I_2(1)P_\xi+J_1\zeta_{0\xi\xi\xi}\right\},\end{aligned}\tag{13}$$

where

$$J_1=\int_0^1\int_y^1\int_0^{y_1}\frac{(U(y_1)-c)^2}{(U(y)-c)^2(U(y_2)-c)^2}dy_2dy_1dy.$$

Integrating by parts gives

$$-2I_{31}\zeta_{0\tau}+3I_{41}\zeta_0\zeta_{0\xi}+J_1\zeta_{0\xi\xi\xi}=\frac{U(0)h_\xi}{U(0)-c}+P_\xi,\tag{14}$$

with $I_{n1}=I_n(1)$, $n=1,2,3,4$. Going back to the fixed-frame x, using the condition that $c=\epsilon f$ while keeping the slow-time $\tau=\epsilon t$, we arrive at the new forced Korteweg-de Vries (fKdV) equation

$$-2I_{31}\zeta_{0\tau}-2I_{31}f\zeta_{0x}+3I_{41}\zeta_0\zeta_{0x}+J_1\zeta_{0xxx}=h_x(x)+P_x(x).\tag{15}$$

When the current is constant throughout the water column, this equation is consistent with that obtained by Grimshaw and Smyth [23] for a pressure distribution. In the absence of a pressure and topography forcing, this fKdV equation is consistent with that obtained by Freedman and Johnson [17] for rotational waves. Note that mathematically the effects of pressure and topography are the same, in the sense that for a undisturbed initial free surface no waves are generated when $P(x)=-h(x)$.

We call attention to the fact that when the condition $c=\epsilon f$ is imposed, we also restrict the admissible shearing currents. In particular we are interested in regimes with a constant vorticity ω. Thus we will consider a shearing current with a linear profile of the form

$$\overline{U}(y)=\Omega y+\beta.$$

The notation is the same as in Freedman and Johnson [17], where $\Omega=-\omega$. Imposing Burns condition for this profile gives

$$1=\int_0^1\frac{1}{(\overline{U}(y)-c)^2}dy=\frac{1}{(\beta-c)(\Omega+\beta-c)},$$

which yields the following admissible wave speeds:

$$c\equiv C^{\pm}(\Omega,\beta)=\beta+\frac{(\Omega\pm\sqrt{\Omega^2+4})}{2}.$$

Our model requires a wave speed of $\mathcal{O}(\epsilon)$. Consider the following *ansatz* for our current:

$$U(y)\equiv\overline{U}(y)-C^-(\Omega,\beta)+\epsilon f=\Omega y-\frac{\Omega}{2}+\frac{\sqrt{\Omega^2+4}}{2}+\epsilon f.$$

Substituting in (9) we find that Burns condition is automatically satisfied with $C = \epsilon f$. Hence we can write that

$$U(y) = \Omega y + \gamma(\Omega) + \epsilon f, \tag{16}$$

where

$$\gamma(\Omega) = -\frac{\Omega}{2} + \frac{\sqrt{\Omega^2 + 4}}{2}.$$

The Froude number is then expressed in the form

$$F(\Omega) = -\frac{\Omega}{2} + \frac{\sqrt{\Omega^2 + 4}}{2} + \epsilon f. \tag{17}$$

For the current given by (16), the coefficients of equation (15) are obtained as

$$I_{31} = \frac{\Omega + 2\gamma(\Omega)}{2\gamma(\Omega)^2(\Omega + \gamma(\Omega))^2}, \quad I_{41} = \frac{1}{3}\frac{\Omega^2 + 3\Omega\gamma(\Omega) + 3\gamma(\Omega)^2}{\gamma(\Omega)^3(\Omega + \gamma(\Omega))^3}, \quad J_1 = \frac{1}{3\gamma(\Omega)^3}. \tag{18}$$

From now on we refer to the vorticity parameter Ω as obtained through (16). This model is our starting point to study long rotational waves, under the effect of constant vorticity, in particular, in the presence of topographic forcing. As the topography gradually increases in amplitude we will eventually need to consider Euler's equations.

3 Potential theory formulation for Euler Equations

In this section we present the formulation for the harmonic component of the velocity in the presence of constant vorticity. We consider a sheared current of constant vorticity in the presence of a pressure distribution and a topography. The problem will be reformulated in terms of the pertubation velocity potential $\tilde{\phi}$. Having this at hand, we can perform a conformal mapping of the irregular flow domain onto a uniform strip.

Consider the pressure distribution to be travelling with speed U_0 along the free surface while the submarine obstacle also travels with speed U_0 along the bottom. The Euler equations are written as:

$$\begin{aligned}
&u_t + uu_x + vu_y = -\frac{p_x}{\rho}, \quad \text{for} \quad -h_0 + h(x + U_0 t) < y < \tilde{\zeta}(x,t),\\
&v_t + uv_x + vv_y = -\frac{p_y}{\rho} - g, \quad \text{for} \quad -h_0 + h(x + U_0 t) < y < \tilde{\zeta}(x,t),\\
&u_x + v_y = 0, \quad \text{for} \quad -h_0 + h(x + U_0 t) < y < \tilde{\zeta}(x,t),\\
&p = P(x + U_0 t), \quad \text{at} \quad y = \tilde{\zeta}(x,t),\\
&v = \tilde{\zeta}_t + u\tilde{\zeta}_x, \quad \text{at} \quad y = \tilde{\zeta}(x,t),\\
&v = h_t + h_x u, \quad \text{at} \quad y = -h_0 + h(x + U_0 t).
\end{aligned} \tag{19}$$

As before, the functions $\tilde{\zeta}, u, v, h$ and p are smooth and decay to zero as $|x| \to \infty$. Consider the velocity field in the form

$$(u, v) = \nabla\tilde{\phi} + (ay, 0), \tag{20}$$

where $\tilde{\phi}$ is the harmonic component and $-a$ is the constant vorticity value. Substitute (20) in (19) to obtain

$$\begin{aligned}
&\Delta\tilde{\phi} = 0, \quad \text{for} \quad -h_0 + h(x+U_0t) < y < \tilde{\zeta}(x,t),\\
&\tilde{\zeta}_t + (a\tilde{\zeta} + \tilde{\phi}_x)\tilde{\zeta}_x - \tilde{\phi}_y = 0, \quad \text{at} \quad y = \tilde{\zeta}(x,t),\\
&\tilde{\phi}_t + \frac{1}{2}(\tilde{\phi}_x^2 + \tilde{\phi}_y^2) + a\tilde{\zeta}\tilde{\phi}_x + \tilde{\zeta} - a\tilde{\psi} = -\frac{P(x+U_0t)}{\rho}, \quad \text{at} \quad y = \tilde{\zeta}(x,t),\\
&(U_0 - ah_0)h_x + ahh_x + \tilde{\phi}_x h_x = \tilde{\phi}_y, \quad \text{at} \quad y = -h_0 + h(x+U_0t).
\end{aligned}$$

By $\tilde{\psi}$ we denote the harmonic conjugate of $\tilde{\phi}$. Now we place ourselves in a moving frame $x \to x + U_0t$ and write

$$\tilde{\zeta}(x - U_0t, t) = \overline{\zeta}(x,t), \quad \tilde{\phi}(x - U_0t, y, t) = \overline{\phi}(x,y,t),$$

to obtain

$$\begin{aligned}
&\Delta\overline{\phi} = 0, \quad \text{for} \quad -h_0 + h(x) < y < \overline{\zeta}(x,t),\\
&\overline{\zeta}_t + (U_0 + a\overline{\zeta} + \overline{\phi}_x)\overline{\zeta}_x - \overline{\phi}_y = 0, \quad \text{at} \quad y = \overline{\zeta}(x,t),\\
&\overline{\phi}_t + \frac{1}{2}(\overline{\phi}_x^2 + \overline{\phi}_y^2) + (U_0 + a\overline{\zeta})\overline{\phi}_x + \overline{\zeta} - a\overline{\psi} = -\frac{P(x)}{\rho}, \quad \text{at} \quad y = \overline{\zeta}(x,t),\\
&(U_0 - ah_0)h_x + ahh_x + \overline{\phi}_x h_x = \overline{\phi}_y, \quad \text{at} \quad y = -h_0 + h(x).
\end{aligned} \tag{21}$$

In this framework, we are prescribing the velocity to having constant vorticity, established through the background flow, while satisfying the Neumann condition around a fixed submarine obstacle. The pressure distribution and the bottom topography are stationary in this reference frame.

3.1 Conformal mapping

In this section we use a conformal mapping taking a uniform (flat) strip onto the fluid domain, containing the submarine obstacle and the respective free surface disturbance. We choose as our reference units in space, speed, time and pressure respectively h_0, $(gh_0)^{1/2}$, $(h_0/g)^{1/2}$ and $\rho g h_0$. We thus rescale (21) in the form

$$\begin{aligned}
&\Delta\overline{\phi} = 0, \quad \text{for} \quad -1 + h(x) < y < \overline{\zeta}(x,t),\\
&(F - \Omega)h_x + \Omega hh_x + \overline{\phi}_x h_x = \overline{\phi}_y, \quad \text{at} \quad y = -1 + h(x),\\
&\overline{\zeta}_t + (F + \Omega\overline{\zeta} + \overline{\phi}_x)\overline{\zeta}_x - \overline{\phi}_y = 0, \quad \text{at} \quad y = \overline{\zeta}(x,t),\\
&\overline{\phi}_t + \frac{1}{2}(\overline{\phi}_x^2 + \overline{\phi}_y^2) + (F + \Omega\overline{\zeta})\overline{\phi}_x + \overline{\zeta} - \Omega\overline{\psi} = -P(x), \quad \text{at} \quad y = \overline{\zeta}(x,t),
\end{aligned} \tag{22}$$

where the Froude number is $F = U_0/(gh_0)^{1/2}$ and $\Omega = ah_0/(gh_0)^{1/2}$. The dimensionless vorticity is given by $-\Omega$.

Consider the conformal mapping from the canonical w-plane ($w = \xi + i\eta$) onto the physical z-plane ($z = x + iy$),

$$z(\xi,\eta,t) = x(\xi,\eta,t) + iy(\xi,\eta,t),$$

satisfying the boundary conditions

$$y(\xi,0,t)=\overline{\zeta}(x(\xi,0,t),t) \;\text{ and }\; y(\xi,-D,t)=-1+H(\xi,t),$$

where $H(\xi,t)=h(x(\xi,-D,t))$. It is required that the canonical strip's height D is a function of time t. $D=D(t)$ depends on the wave profile and will be determined later.

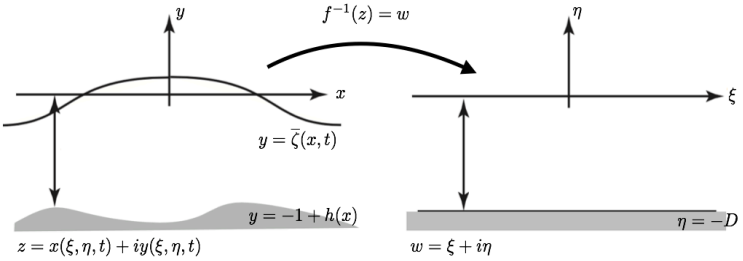

Figure 1: The inverse conformal mapping at a given time t. Both the free surface and the bottom topography are flattened out.

For this complex-variables formulation drop the bar from the velocity potential $\overline{\phi}$. In the canonical domain, the harmonic conjugate of $\phi=\phi(\xi,\eta,t)$ is denoted by $\psi=\psi(\xi,\eta,t)$. We denote by $\Phi(\xi,t)$ and $\Psi(\xi,t)$ their traces along the canonical free surface $\eta=0$. Under the mapping, the image of $\eta=0$ is the physical free surface elevation, parametrized as $\mathrm{X}(\xi,t)$ and $\mathrm{Y}(\xi,t)$. Using these functions in the Bernoulli and kinematic conditions from (22), and proceeding as in [30], we obtain

$$\begin{aligned}
&\mathrm{Y}_t=\mathrm{Y}_\xi\mathcal{C}\left[\frac{\Theta_\xi}{J}\right]-\mathrm{X}_\xi\frac{\Theta_\xi}{J},\\
&\Phi_t=-\mathrm{Y}-\frac{1}{2J}(\Phi_\xi^2-\Psi_\xi^2)+\Phi_\xi\mathcal{C}\left[\frac{\Theta_\xi}{J}\right]-\frac{1}{J}(F+\Omega\mathrm{Y})\mathrm{X}_\xi\Phi_\xi+\Omega\Psi-P(\mathrm{X}),
\end{aligned}\tag{23}$$

where $\Theta_\xi(\xi,t)=\Psi_\xi+F\mathrm{Y}_\xi+\Omega\mathrm{Y}\mathrm{Y}_\xi$. The operator $\mathcal{C}[\cdot]$ is defined as follows: given a function $f(\xi)$ we have

$$\mathcal{C}[f(\xi)]=\mathcal{C}_0[f(\xi)]+\lim_{k\to0} i\coth(kD)\widehat{f}(k),\tag{24}$$

where $\mathcal{C}_0[\cdot]=\mathcal{F}^{-1}\mathcal{H}\mathcal{F}[\cdot]$. The Fourier transform is denoted by $\mathcal{F}$, with $\mathcal{F}[f]=\widehat{f}$. The Fourier multiplier $\mathcal{H}$ is defined as

$$\mathcal{H}(k)=\begin{cases} i\coth(kD), & \text{if } k\neq0,\\ 0, & \text{if } k=0.\end{cases}$$

In particular if $f_\xi(\xi)$ is well defined, we have that

$$\mathcal{C}[f(\xi)]=\mathcal{C}_0[f_\xi(\xi)]-\frac{\widehat{f}(0)}{D}.$$

Since $x(\xi,\eta)$ and $y(\xi,\eta)$ are harmonic conjugates, one obtains that [30]

$$\mathrm{X}_t=\mathrm{X}_\xi\mathcal{C}\left[\frac{\Theta_\xi(\xi,t)}{J}\right]+\mathrm{Y}_\xi\frac{\Theta_\xi(\xi,t)}{J}.\tag{25}$$

At this stage we have three harmonic problems at hand. First, due to the conformal mapping,

$$\begin{aligned}
&y_{\xi\xi} + y_{\eta\eta} = 0, \quad \text{for} \quad -D < \eta < 0,\\
&y = \mathrm{Y}(\xi, t), \quad \text{at} \quad \eta = 0,\\
&y = -1 + H(\xi, t), \quad \text{at} \quad \eta = -D,
\end{aligned}$$

where the Dirichlet boundary conditions express the top and bottom corrugations in the fluid domain. In the canonical domain, the harmonic component of the velocity field satisfies

$$\begin{aligned}
&\phi_{\xi\xi} + \phi_{\eta\eta} = 0, \quad \text{for} \quad -D < \eta < 0,\\
&\phi = \Phi(\xi, t), \quad \text{at} \quad \eta = 0,\\
&\phi_\eta = (F - \Omega) H_\xi + \Omega H H_\xi, \quad \text{at} \quad \eta = -D.
\end{aligned}$$

Using the Cauchy-Riemann equations with its harmonic conjugate along the bottom $\eta = -D$, we have that

$$\begin{aligned}
&\psi_{\xi\xi} + \psi_{\eta\eta} = 0, \quad \text{for} \quad -D < \eta < 0,\\
&\psi = \Psi(\xi, t), \quad \text{at} \quad \eta = 0,\\
&\psi = -(F - \Omega) H - \frac{\Omega}{2} H^2 + Q, \quad \text{at} \quad \eta = -D.
\end{aligned}$$

Q is a function that depends only on time t. The three Laplace problems above are linear. Their solutions are given by Fourier transforms:

$$\begin{aligned}
y(\xi, \eta, t) &= \mathcal{F}^{-1}\left[\left(\widehat{\mathrm{Y}} - \frac{\widehat{H}}{\cosh(kD)}\right)\frac{\sinh(k(D+\eta))}{\sinh(kD)} + \frac{\widehat{H}}{\cosh(kD)}\cosh(k\eta)\right] + \frac{\eta}{D},\\
\phi(\xi, \eta, t) &= \mathcal{F}^{-1}\left[\frac{\cosh(k(D+\eta))}{\cosh(kD)}\widehat{\Phi} + \frac{i(F-\Omega)\widehat{H} + i\frac{\Omega}{2}\widehat{H^2}}{\cosh(kD)}\sinh(k\eta)\right],\\
\psi(\xi, \eta, t) &= \mathcal{F}^{-1}\left[\left(\widehat{\Psi} + \frac{(F-\Omega)\widehat{H} + \frac{\Omega}{2}\widehat{H^2}}{\cosh(kD)}\right)\frac{\sinh(k(D+\eta))}{\sinh(kD)}\right.\\
&\qquad\left. - \frac{(F-\Omega)\widehat{H} + \frac{\Omega}{2}\widehat{H^2}}{\cosh(kD)}\cosh(k\eta)\right] - \frac{Q}{D}\eta.
\end{aligned} \tag{26}$$

Using the Cauchy-Riemann relations $x_\xi = y_\eta$, $\phi_\eta = -\psi_\xi$ at $\eta = 0$, we have that

$$\begin{aligned}
\mathrm{X}_\xi(\xi, t) &= \frac{1}{D} + \mathcal{F}^{-1}\left[-i\coth(kD)\left(\widehat{\mathrm{Y}}_\xi(k,t) - \frac{\widehat{H}_\xi(k,t)}{\cosh(kD)}\right)\right],\\
\Phi_\xi(\xi, t) &= \mathcal{F}^{-1}\left[-i\coth(kD)\left(\widehat{\Psi}_\xi(k,t) + \frac{(F-\Omega)\widehat{H}_\xi(k,t) + \frac{\Omega}{2}\widehat{\partial_\xi H^2}(k,t)}{\cosh(kD)}\right)\right].
\end{aligned} \tag{27}$$

Along the bottom $\eta = -D$ we have that

$$x_\xi(\xi, -D, t) = \frac{1}{D} - \mathcal{C}\left[\mathcal{F}^{-1}\left(\frac{\widehat{\mathrm{Y}}_\xi}{cosh(kD)} - \frac{\widehat{H}_\xi}{\cosh^2(kD)}\right)\right] + \mathcal{T}\big[H_\xi\big], \tag{28}$$

where

$$\mathcal{T}\big[H_\xi\big] = \mathcal{F}^{-1} i\tanh(kD)\mathcal{F}\big[H_\xi\big].$$

Next we average $(27)_1$ over our interval of interest:

$$\big\langle \mathrm{X}_\xi(\cdot,t)\big\rangle = \frac{1+\big\langle \mathrm{Y}(\cdot,t)\big\rangle - \big\langle H(\cdot,t)\big\rangle}{D}.$$

We use this condition to impose that the wavelengths are the same in both the physical and canonical domains. In the periodic case this is the same as keeping the period unchanged in both domains [3]. The free surface is changing due to the wave generation and propagation. Since the mapping is conformal and the horizontal length-scale remains unchanged, the vertical (height) of the canonical strip has to adjust accordingly. This is expressed by the time variations of D, which needs to satisfy

$$D = 1 + \big\langle \mathrm{Y}(\cdot,t)\big\rangle - \big\langle H(\cdot,t)\big\rangle. \tag{29}$$

Keeping this in mind, from (23) and (27) we have therefore accomplished the formulation of the Euler equations in the canonical domain:

$$\begin{aligned}
\mathrm{X}_\xi &= \frac{1}{D} - \mathcal{C}\bigg[\mathrm{Y}_\xi - \mathcal{F}^{-1}\bigg(\frac{\widehat{H}_\xi(k,t)}{\cosh(kD)}\bigg)\bigg],\\
\Phi_\xi &= -\mathcal{C}\bigg[\Psi_\xi(\xi,t) + \mathcal{F}^{-1}\bigg(\frac{(F-\Omega)\widehat{H}_\xi(k,t) + \frac{\Omega}{2}\widehat{\partial_\xi H^2}(k,t)}{\cosh(kD)}\bigg)\bigg],\\
\mathrm{Y}_t &= \mathrm{Y}_\xi\mathcal{C}\bigg[\frac{\Theta_\xi}{J}\bigg] - \mathrm{X}_\xi\frac{\Theta_\xi}{J},\\
\Phi_t &= -\mathrm{Y} - \frac{1}{2J}(\Phi_\xi^2 - \Psi_\xi^2) + \Phi_\xi\mathcal{C}\bigg[\frac{\Theta_\xi}{J}\bigg] - \frac{1}{J}(F+\Omega\mathrm{Y})\mathrm{X}_\xi\Phi_\xi + \Omega\Psi - P(\mathrm{X}).
\end{aligned} \tag{30}$$

The topography will appear in the equations as a composition in the form $\mathrm{H}(\xi,t) = h(\mathrm{X}_b(\xi,t))$, where X_b is the bottom trace of $X(\xi,\eta)$. This composite form of the topography satisfies an implicit relation which needs to be calculated in an iterative fashion. From (28), and the definition of the operator $\mathcal{C}$, we have the additional equations

$$\begin{aligned}
&\mathrm{H}(\xi,t) = h(\mathrm{X}_b(\xi,t)),\\
&\mathrm{X}_b(\xi,t) = \xi - \mathcal{C}_0\bigg[\mathcal{F}^{-1}\bigg(\frac{\widehat{\mathrm{Y}}}{\cosh(kD)} - \frac{\widehat{H}}{\cosh^2(kD)}\bigg)\bigg] + \mathcal{T}\big[H\big].
\end{aligned} \tag{31}$$

In the flat bottom case equations (30)-(31) are compatible with those obtained by Choi [30]. As in the flat bottom case, to solve the present system of differential equations we need the initial conditions $\mathrm{Y}(\xi,0)$ and $\Phi(\xi,0)$. Equation $(30)_4$ indicates that we also need the initial value $\Psi(\xi,0)$. Therefore we present the steps in obtaining $\Psi(\xi,t)$ from $\Phi(\xi,t)$. From equation $(30)_2$, for $k\neq 0$, we may write

$$\widehat{\Psi}(k,t) = i\tanh(kD)\widehat{\Phi}(k,t) - \frac{(F-\Omega)\widehat{H}(k,t) + \frac{\Omega}{2}\widehat{H^2}(k,t)}{\cosh(kD)}.$$

We also have that

$$k\coth(kD)\widehat{\Psi}(k,t) = \widehat{\Phi}_\xi(k,t) - \frac{(F-\Omega)\widehat{H}(k,t) + \frac{\Omega}{2}\widehat{H^2}(k,t)}{\cosh(kD)}k\coth(kD).$$

Letting $k \to 0$ yields

$$\widehat{\Psi}(0,t) = D\widehat{\Phi}_\xi(0,t) - (F-\Omega)\widehat{H}(0,t) + \frac{\Omega}{2}\widehat{H^2}(0,t).$$

We have thus obtained $\widehat{\Psi}(k,t)$ from $\widehat{\Phi}(k,t)$.

Another fact of interest from equation (30), is the need to establish the limit

$$\lim_{k\to 0} i\coth(kD)\mathcal{F}\Big[\frac{\Theta_\xi}{J}\Big](k,t).$$

One way to proceed is by observing that $\Theta_\xi(\xi,t)$ and J are smooth, and that $J \neq 0$. These infer the existence of a well defined $M(\xi,t)$, where

$$M_\xi(\xi,t) = \frac{\Theta_\xi(\xi,t)}{J}.$$

Uniqueness of $M(\cdot,t)$ is not guaranteed, unless an initial condition is provided. Imposing an average value $\big\langle M(\cdot,t)\big\rangle$ establishes uniqueness. From equation (25) we can determine a condition for $\big\langle M(\cdot,t)\big\rangle$. From the definition of the operator $\mathcal{C}$ we have that

$$\mathrm{X}_t = \mathrm{X}_\xi \mathcal{C}_0\left[\frac{\Theta_\xi(\xi,t)}{J}\right] + \mathrm{Y}_\xi\frac{\Theta_\xi(\xi,t)}{J} - \mathrm{X}_\xi(\cdot,t)\frac{\big\langle M(\cdot,t)\big\rangle}{D}.$$

Averaging both sides,

$$\big\langle \mathrm{X}_t(\cdot,t)\big\rangle = \left\langle \mathrm{X}_\xi \mathcal{C}_0\left[\frac{\Theta_\xi}{J}\right] + \mathrm{Y}_\xi\frac{\Theta_\xi}{J}\right\rangle(\cdot,t) - \big\langle \mathrm{X}_\xi(\cdot,t)\big\rangle\frac{\big\langle M(\cdot,t)\big\rangle}{D},$$

which results in

$$\big\langle M(\cdot,t)\big\rangle = \frac{D}{\big\langle \mathrm{X}_\xi(\cdot,t)\big\rangle}\left\langle \mathrm{X}_\xi \mathcal{C}_0\left[\frac{\Theta_\xi}{J}\right] + \mathrm{Y}_\xi\frac{\Theta_\xi}{J}\right\rangle(\cdot,t) - D\frac{\big\langle \mathrm{X}_t(\cdot,t)\big\rangle}{\big\langle \mathrm{X}_\xi(\cdot,t)\big\rangle},$$

namely the condition for $M(\cdot,t)$ being unique. Therefore

$$\lim_{k\to 0} i\coth(kD)\mathcal{F}\Big[\frac{\Theta_\xi}{J}\Big](k,t) = -\frac{1}{\big\langle \mathrm{X}_\xi(\cdot,t)\big\rangle}\left\langle \mathrm{X}_\xi \mathcal{C}_0\left[\frac{\Theta_\xi}{J}\right] + \mathrm{Y}_\xi\frac{\Theta_\xi}{J}\right\rangle(\cdot,t) + \frac{\big\langle \mathrm{X}_t(\cdot,t)\big\rangle}{\big\langle \mathrm{X}_\xi(\cdot,t)\big\rangle}.$$

From equations $(30)_1$ and (29) it turns out that

$$\mathrm{X}(\xi,t) = \xi - \mathcal{C}_0\left[\mathrm{Y} - \mathcal{F}^{-1}\left(\frac{\widehat{H}(k,t)}{\cosh(kD)}\right)\right].$$

This leads to $\big\langle \mathrm{X}_t(\cdot,t)\big\rangle = 0$ and consequently

$$\lim_{k\to 0} i\coth(kD)\mathcal{F}\Big[\frac{\Theta_\xi}{J}\Big](k,t) = -\left\langle \mathrm{X}_\xi \mathcal{C}_0\left[\frac{\Theta_\xi}{J}\right] + \mathrm{Y}_\xi\frac{\Theta_\xi}{J}\right\rangle(\cdot,t).$$

4 Numerical methods and results

In this section we consider simulations of the fKdV model (15) and the Euler system (30)-(31). We will approximate solutions on the real line with a large periodic domain. We use a Fourier pseudospectral method to numerically solve the fKdV equation with an integrating factor for the linear part, thus avoiding numerical problems due to the higher order dispersive term [15, 19]. For the Euler system we do not use an integrating factor. Fourier transforms are approximated by the Fast Fourier Transform (FFT) on a uniform grid and all derivatives are performed in Fourier space.

The numerical approximation to the solution of the fKdV equation is found on a computational domain $x \in [-L_K, L_K)$, with N_K uniformly spaced points with grid size $\Delta x_K = 2L_K/N_K$. Fourth order Runge-Kutta is used for time integration on an interval $\tau \in [0, T_K]$ using a timestep $\Delta\tau_K$. For the Euler system in the canonical variables the computational domain is $\xi \in [-L_E, L_E)$, with N_E uniformly spaced points with grid size $\Delta\xi_E = 2L_E/N_K$. This corresponds to a nonuniform (and time varying) grid in physical space. Fourth order Runge-Kutta is used for time integration on an interval $t_E \in [0, T_E]$ using a timestep Δt_E.

The derivation of the KdV equation assumes an asymptotic limit $\epsilon \to 0$. Our comparisons with the Euler system will be for small but finite values of ϵ (typically $\epsilon = 0.1$) and the transformation between the scaled KdV variables and the unscaled Euler variables needs to be taken into account in order to compare solutions. For the nearly resonant flows ($F = 1 + \epsilon f$) that we consider in this paper, the transformations are as follows:

$$x_E = \epsilon^{-1/2} x_K, \quad t_E = \epsilon^{-3/2}\tau_K, \quad \zeta_E = \epsilon^{-1}\zeta_K, \quad h_E = \epsilon^2 h_K.$$

To compare a KdV solution on $[-L_K, L_K) \times [0, T_K]$, to an Euler system solution, the computational domain for Euler system must be much larger, requiring $L_E = \epsilon^{-1/2} L_K$ and $T_E = \epsilon^{-3/2} T_K$. In general, we set $\Delta\xi_E = \Delta x_K$ which, modulo the domain rescaling, provides the same spectral *resolution*. The implementation was carried out with an FFT. As ϵ increases, the forcing is stronger and the solutions to the Euler equations become more nonlinear, with a wider wavenumber band, and in some cases leading to the onset of wave-breaking. In this case the Euler grid size needs to be much smaller than for the KdV regime. Naturally, the solution to the KdV equation is independent of ϵ.

For the Euler system, (31) shows that $\mathrm{X}_b(\xi, t)$ and $H(\xi, t)$ are coupled in a nontrivial fashion. In order to advance with the Runge-Kutta timestep we need to know, beforehand, the coefficient $H(\xi, t_m)$ at the given stage in time. The following iterative scheme is used to compute it:

$$\begin{aligned} \mathrm{X}_b^l(\xi, t_m) &= \xi - \mathcal{C}_0\left[\mathcal{F}^{-1}\left(\frac{\widehat{\Upsilon}(k, t_m)}{cosh(kD)} - \frac{\widehat{H}^l(k, t_m)}{cosh^2(kD)}\right)\right] + \mathcal{T}\big[H^l(\xi, t_m)\big], \\ H^{l+1}(\xi, t_m) &= h(\mathrm{X}_b^l(\xi, t_m)). \end{aligned} \tag{32}$$

The initial step is $\mathrm{X}_b^0(\xi, t_m) = \mathrm{X}_b(\xi, t_{m-1})$ and $H^1(\xi, t_m) = H(\xi, t_{m-1})$ This scheme is performed at every time step, with the stopping criteria

$$\max_{\xi \in [-L, L]} \big|H^{l+1}(\xi, t_m) - H^l(\xi, t_m)\big| < \delta,$$

where δ is a given tolerance.

4.1 Simulations in the fKdV regime

The fKdV model is in a regime where wave generation due to a pressure distribution is analogous to that by a submarine obstacle. Mathematically, the forcing terms are identical. Grimshaw and Smyth [22] compared the irrotational solutions of the fKdV model with the Euler equations in the case of a moving pressure distribution along the free surface. In the present work we explored nearly-resonant wave forms, generated mostly due to topographic forcing. Our potential theory formulation, for the Euler equations with vorticity, is solved numerically in the canonical domain. We initially compared its numerical results with the weakly dispersive, weakly nonlinear fKdV model. In the regime where solutions are expected to match we observed an excellent numerical agreement. For a proper comparison a rescaling of numerical solutions is performed. Both models start from zero initial data, namely with the channel at rest, with a bottom topography described by $h_K(x_K) = (1/\pi^{1/2})\, e^{-x_K^2}$ in the fKdV model and by $h_E(x_E) = (\epsilon^2/\pi^{1/2})\, e^{-\epsilon x_E^2}$ in the Euler system. All simulations are carried out on a spatial grid with $\Delta x_K = \Delta \xi_E = 0.1$ and $N = 2^{14}$ grid points and $\Delta\tau = \Delta t = 0.01$. Periodic boundary conditions are used at the end of the computational domain. In all figures only the part of the computational domain, containing wave activity, is shown.

We performed numerical simulations in the irrotational regime for Froude numbers in the three nearly-resonant regimes: critical, supercritical and subcritical. The figures that follow will be useful for identifying for regimes in the rotational case, where the critical Froude number is no longer equal to 1. The small amplitude topography is fixed by imposing $\epsilon = 0.1$. The agreement between the respective KdV solution and the solution to Euler equations is very good. A snapshot of a well-developed solution in time, is provided for each regime.

In figure 2 we compare both models in the critical ($F = 1 + \varepsilon f;\ f = 0$) case. We can see the downstream oscillatory wave train, the lower free surface level behind the obstacle and the zero free surface level in the upstream far field. Downstream the fKdV wave crests are progressively ahead from those of the Euler system solution, due to their different dispersion relations. The wave pattern upstream is very similar, with a slow periodic pulse emission. Due to the slow pulse emission, in the bottom figure we display the solution at a later time. The wave profiles are essentially the same, but the different dispersion relations are manifested through a small phase-lag. In the following supercritical case we will see a stationary pulse above the topography.

In figure 3 we consider a supercritical simulation with $f = 0.75$. We observe a dominant wave stationed exactly above the topography, centered at the origin, while a smaller transient wavetrain moves downstream. The fKdV wavetrain is slightly ahead of the respective Euler-wavetrain. In figure 4 we consider a subcritical case with $f = -0.5$, where the onset of a dispersive shock now appears. The developing downstream shock, as time increases, yields a limiting state of steady periodic lee waves. These three figures will be useful in identifying regimes in the rotational case, where the critical Froude number is shifted.

We allowed for a gradual increase of the topography's amplitude. We tested this for both types of forcing, namely due to the pressure distribution and the bottom topography. The forcing increased gradually and drove the two models into different wave profiles. When we used $\epsilon = 0.075^{1/2} \approx 0.274$, still not a large value, the solutions were not matching as before. In some cases we observed the onset of wave breaking. Recently, using an extended (fifth-order) fKdV irrotational model, Albalwi, Marchant and Smyth [16] showed numerical results where they infer the presence of a dispersive shock. They compared solutions of their eKdV model (e for extended) with those of the fKdV model. We observed a similar scenario, using the full irrotational Euler model for comparison. As observed with our Euler equation solutions, Albalwi, Marchant and Smyth [16] point out that the spatial extent of the eKdV's

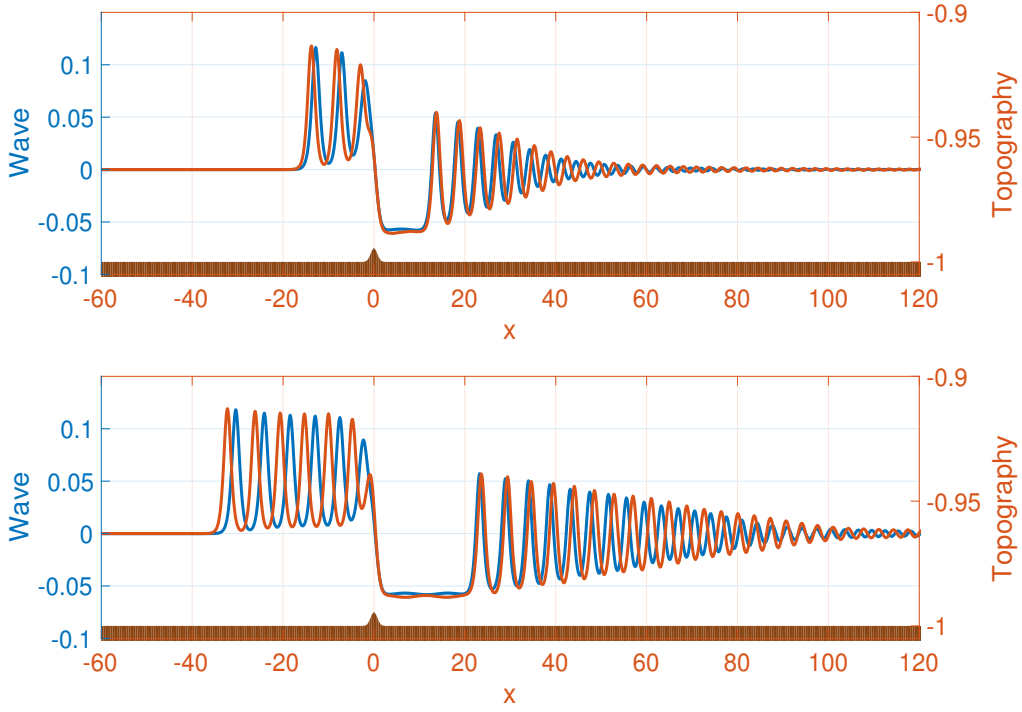

Figure 2: Critical case ($F = 1 + \varepsilon f; f = 0$): the free surface disturbances at times $\tau = 30$ (top) and $\tau = 60$ (bottom). The perturbation amplitude is $\epsilon = 0.1$. The topography is centered about $x = 0$ and the background flows to the right. In red we display the fKdV solution and in blue (darker line) the Euler solution.

oscillatory wave train is shorter than that for the fKdV. Eventually undular bores can form. Dispersive shocks is a theme on its own right and beyond the scope of the present study.

4.2 Rotational-wave generation

We now add the sheared current in the presence of topography, a scenario not explored before. Adopting the vorticity-dependent Froude number $F(\omega)$, given by (17), the agreement between the fKdV and Euler models only depends on the topography amplitude, as before. Hence the topography amplitude is slightly increased and we position ourselves beyond the KdV-regime. We recall that in the physical domain the topography is represented as $h(x) = \epsilon^2 \exp(-0.1x^2)$, namely a Gaussian mound centered at the origin. Within the fKdV scaling this forcing term given by $h(x) = \exp((-0.1/\epsilon^{1/2})x^2)$. The topography amplitude is now taken as $\epsilon^2 = 0.075$ (where $\varepsilon = 0.274$).

As will be shown, in the critical regime positive vorticity ($\omega > 0$) is adverse while negative vorticity is favorable, namely by acting against wave breaking. Recall from (17) that the critical regime refers to $f = 0$ and not necessarily $F = 1$.

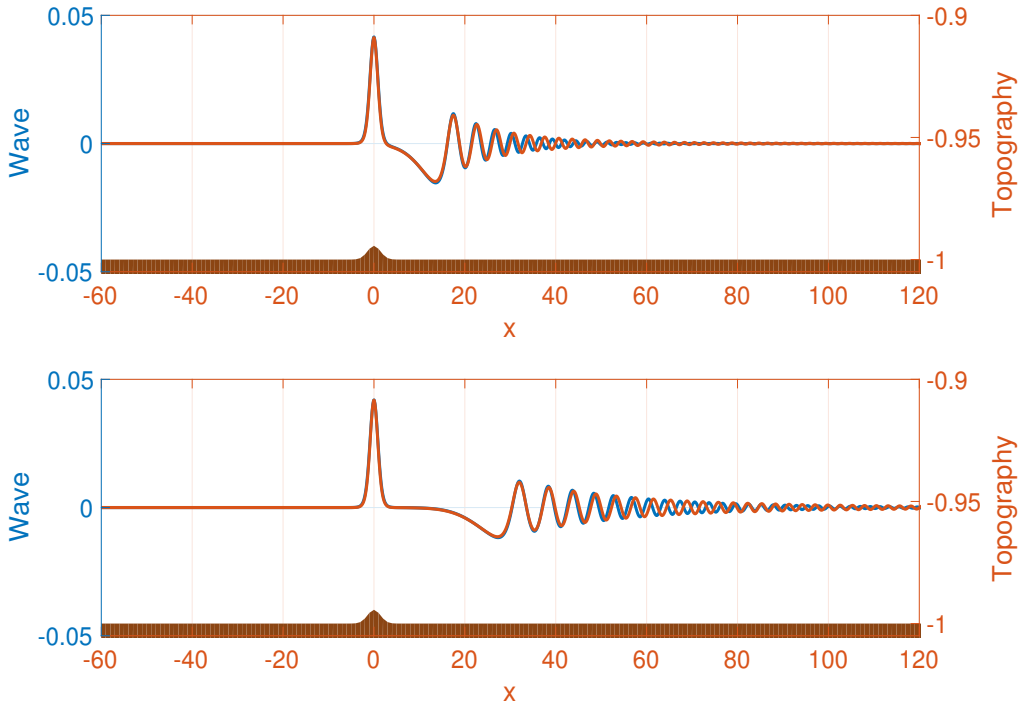

Figure 3: Supercritical case ($F = 1 + \varepsilon f = 1.075$; $\epsilon = 0.1$, f=0.75): the free surface disturbances at times $\tau = 15$ (top) and $\tau = 30$ (bottom). The topography is centered about $x = 0$ and the background flows to the right. In red we display the fKdV solution and in blue (darker line) the Euler solution.

In figures 5 and 6 we display different critical regimes, due to the use of different values of the vorticity ω. We compare fKdV solutions with Euler solutions for both positive and negative vorticities. The respective critical regime varies according to F_ω given by (33) below or earlier at (17). For positive vorticities, in figure 5, we clearly see that both upstream and downstream Euler waves are steeper than those for the fKdV. This is also true in the case of negative vorticity. We remark that the (negative vorticity) Euler solutions displayed in figure 6 are smoother, and have run for a longer time interval, when compared with the respective (positive vorticity) Euler solutions in figure 5. Hence we call $\omega < 0$ a favorable vorticity regime. In figure 5 we observe that as $\omega > 0$ decreases, the wave steepness is reduced. On the other hand for negative vorticity, as its intensity increases the wave steepness decreases. Hence negative vorticity has a smoothing effect.

The rotational fKdV (15) has its regimes controlled through f, the Froude number's perturbation to the resonant regime. While deducing (15) we have established a relationship between the vorticity and the Froude number, as given in (17). With the Euler equations we may vary these two parameters independently. In the following Euler equation simulations we fix a Froude number F while allowing for different vorticity values and therefore, different underlying critical F_ω given by (33).

In figure 7 we set $F = 1$ (the irrotational critical value) and compare three different vorticity values:

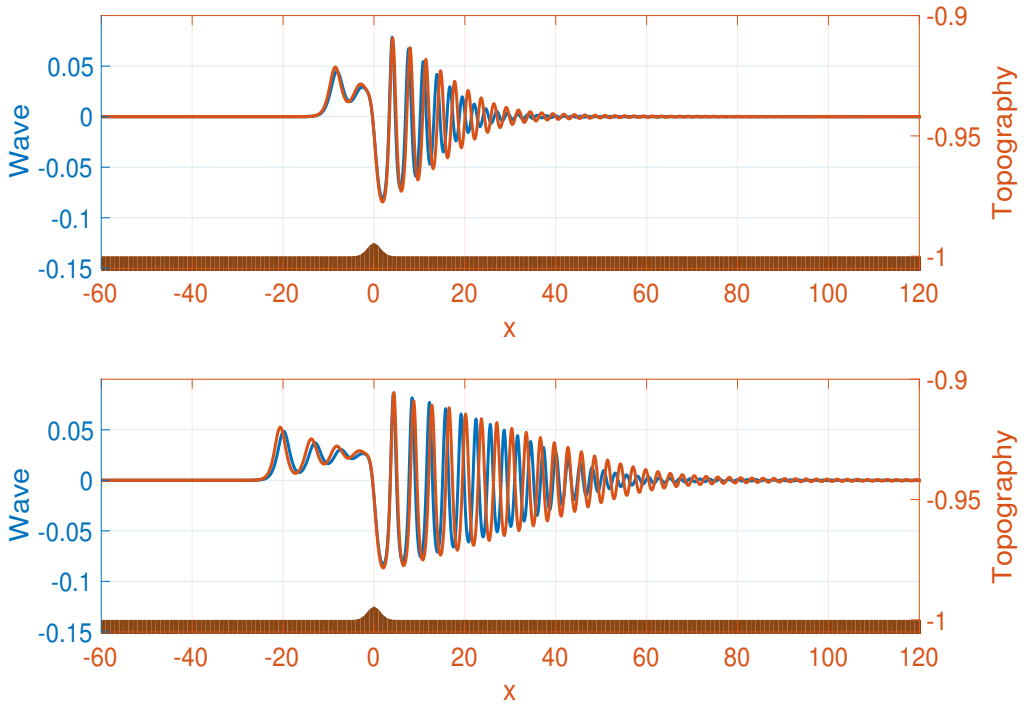

Figure 4: Subcritical case ($F = 1 + \varepsilon f = 0.95$; $\epsilon = 0.1$, $f = -0.50$): the free surface disturbances at times $\tau = 15$ (top) and $\tau = 30$ (bottom). The topography is centered about $x = 0$ and the background flows to the right. In red we display the fKdV solution and in blue (darker line) the Euler solution.

$\omega = -0.5, 0, +0.5$. These correspond respectively to $F_\omega = 0.7808, 1, 1.2808$. The dashed line represents the irrotational wave profile, which is in the critical regime. Qualitatively the wave profile is similar to that displayed in figure 2. For the negative vorticity we have $F_\omega = 0.7808$ and therefore $F = 1$ should be supercritical. This is confirmed, as we compare qualitatively the respective wave profile from figure 7 with that from figure 3. We have a pulse stationed above the topography. Finally for the positive vorticity we have $F_\omega = 1.2808$ and therefore $F = 1$ should be subcritical. This is corroborated by comparing qualitatively with figure 4.

Next we consider $F = 1.1$, which is a supercritical irrotational case. Results are depicted in figure 8 and again vorticity is capable of changing the regime. Remarkably the solution for the negative vorticity behaves in a subcritical regime, with a transient propagating upstream and an oscillatory wavetrain propagating downstream, qualitatively similar to figure 4. We also considered the subcritical $F = 0.9$ case, having similar profiles which are not here displayed. For a positive vorticity value ($\omega = 0.5$) we observed a shift in the regime. A stationary pulse is observed over the topography, in an effective supercritical regime.

For the irrotational case we verified numerically the onset of wave breaking for solutions to Euler's equations when $F \in [0.7, 1.2]$. Away from this critical interval, containing the critical Froude number

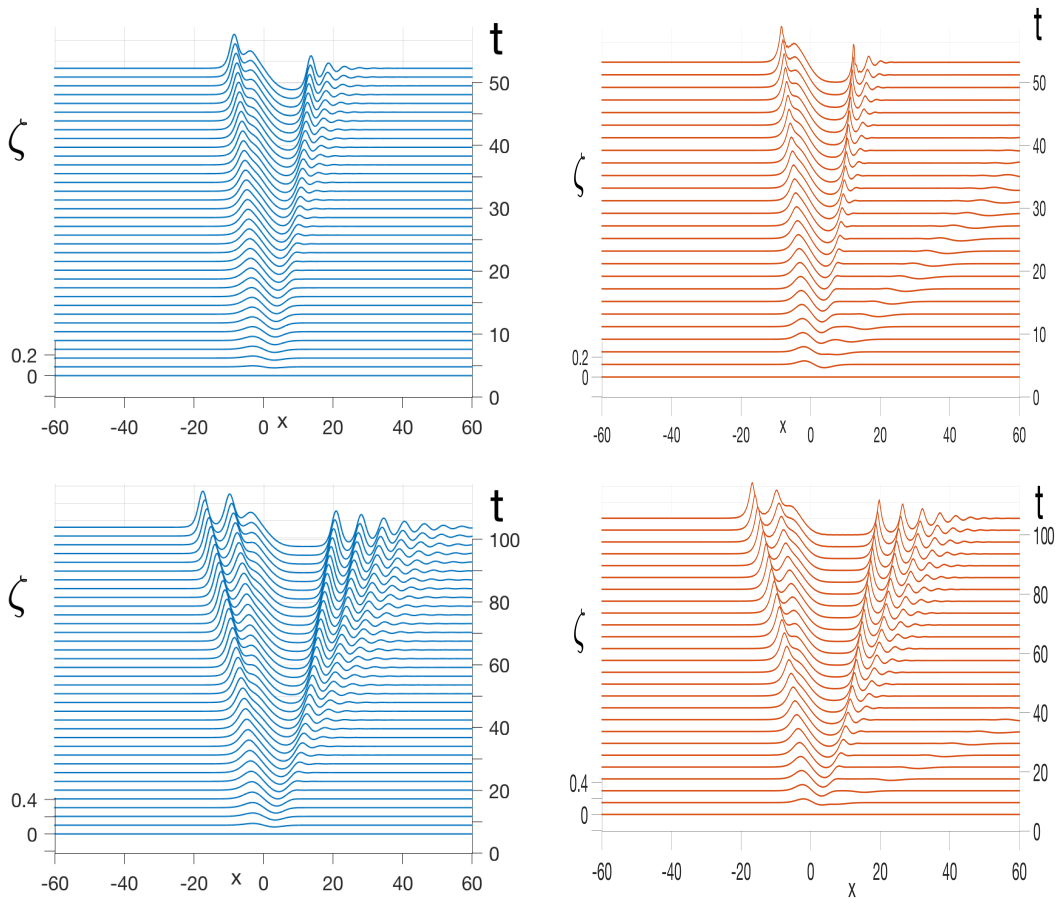

Figure 5: Critical rotational regimes: solution evolution for the fKdV equation (left; with $f = 0$) and the Euler equations (right; with $F = F_\omega$). The topographic forcing has amplitude $\varepsilon^2 = 0.075$ and is centered at the origin $x = 0$. From top to bottom each row has a different constant vorticity: $\omega = 0.5, 0.1$ with the respective (underlying) critical Froude number given in (17) or (33): $F_\omega = 0.7808, 0.9512$. The Euler solutions are sharper crested than the KdV solutions.

$F = 1$, waves were not observed to break. In the presence of vorticity we have numerically noticed that this critical interval is shifted. Denoting the critical rotational Froude number as F_ω, from (17) we have that:

$$F_\omega = \frac{\omega}{2} + \frac{\sqrt{\omega^2 + 4}}{2}. \tag{33}$$

Numerical evidence indicates that the critical interval, for rotational wave breaking, is given by

$$F \in \Big[F_\omega - 0.3, F_\omega + 0.2\Big].$$

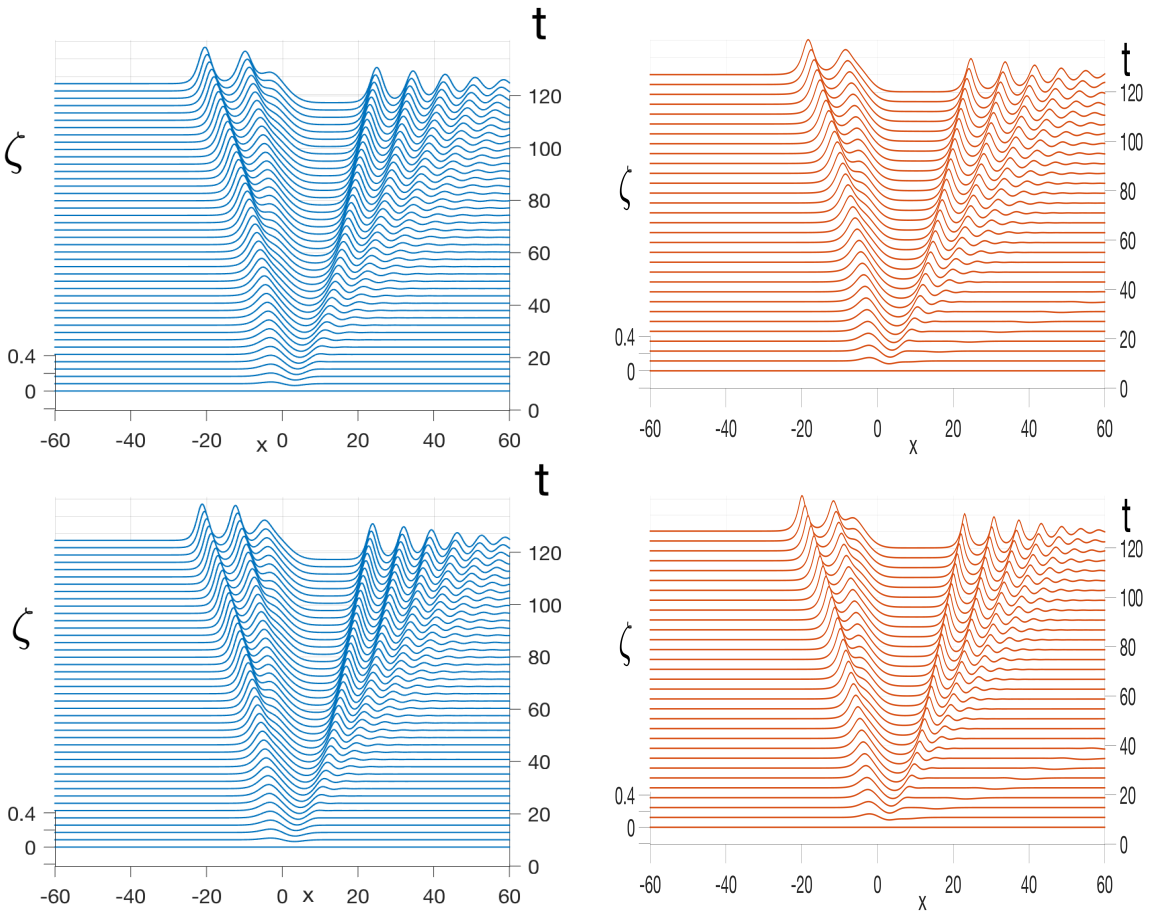

Figure 6: Critical rotational regimes, with negative vorticity: solution evolution for the fKdV equation (left; with $f = 0$) and for the Euler equations (right; with $F = F_\omega$). The topographic forcing has amplitude $\varepsilon^2 = 0.075$ and is centered at the origin $x = 0$. From top to bottom each row has a different constant vorticity: $(\omega = -0.5, -0.1)$ with the respective (underlying) critical Froude number given in (17) or (33): $F_\omega = 1.2808, 1.0512$. The Euler solutions are sharper crested than the KdV solutions.

Wave breaking and dispersive shocks is a theme a current interest but beyond the scope of the present work. Equation (33) provides a curve of critical Froude numbers in the $\omega \times F$ plane. In figure 9 we display the Euler dispersion relation curve for three different vorticity values. The uniform background flow is taken as zero. Note that in the long-wave limit the phase speed coincides with the respective critical Froude numbers F_ω, for respectively $\omega = -0.5$ and $\omega = 0.5$.

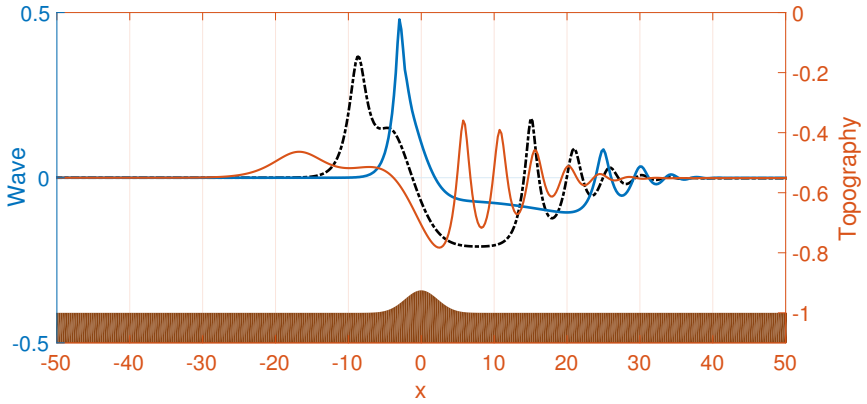

Figure 7: $F = 1$ case: Euler solutions at $t = 60$. The (black) dashed line displays the critical ($F = 1$) irrotational solution. To its right (in blue) the $\omega = 0.5$ ($F_\omega = 0.7808 < F$) supercritical solution and to the left (in red) the $\omega = -0.5$ ($F_\omega = 1.2808 > F$) subcritical solution. The critical, supercritical and subcritical patterns are qualitatively similar to figures 2-4 respectively. The topography is centered at the origin $x = 0$, where $\epsilon = 0.075^{1/2} \approx 0.274$.

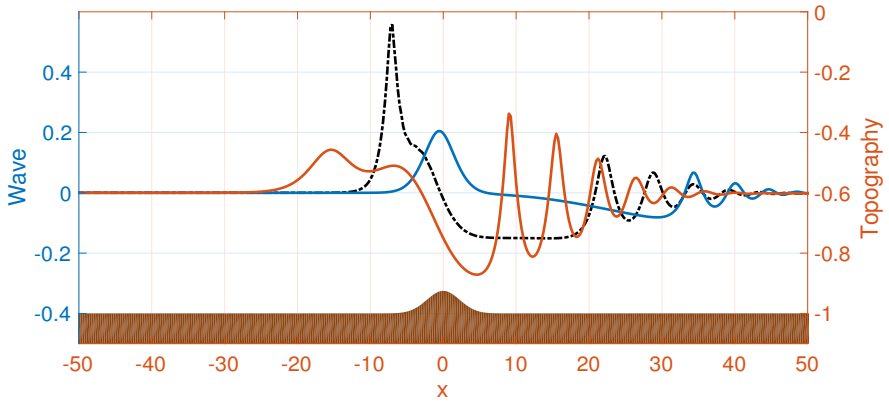

Figure 8: $F = 1.1$ case: Euler solutions at $t = 70$. The (black) dashed line displays the supercritical ($F = 1.1$) irrotational solution. To its right (in blue) the $\omega = 0.5$ ($F_\omega = 0.7808 < F$) supercritical solution and to the left (in red) the $\omega = -0.5$ ($F_\omega = 1.2808 > F$) subcritical solution. The critical, supercritical and subcritical patterns are qualitatively similar to figures 2-4 respectively. The topography is centered at the origin $x = 0$, where $\epsilon = 0.075^{1/2} \approx 0.274$.

5 Stability of stationary solutions

In this section we look for stationary solutions in both the irrotational and rotational cases. Instead of starting with the undisturbed free surface, as before, we now set the initial data equal to the stationary solution found by a Newton-type method. We then verify that the evolution scheme does not alter

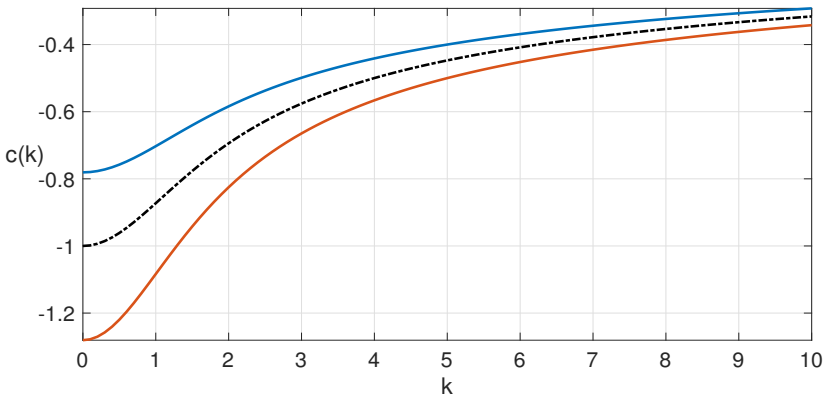

Figure 9: Dispersion relation for the Euler equations at different vorticity values ω. The dashed curve is the irrotational case. The blue line (above it) refers to $\omega = 0.5$, while the red line (below) to $\omega = -0.5$.

the respective stationary wave. We then perturb the initial (stationary) wave profile and numerically observe if these solutions are stable.

For the fKdV equation, stationary waves and their related stability properties were studied in [20, 21, 9]. More recently Grimshaw and Maleewong [22] studied the stability of stationary fKdV solutions in both the subcritical and supercritical regimes. They found their stationary wave from the transient fKdV solution, whose stability was then analyzed through the Euler equations in the presence of a moving pressure distribution. In the presence of a constant current and a topography, Vanden-Broeck [12] used a boundary integral method to compute stationary solutions to the Euler equations. Different stationary waves were found but their stability was not analyzed numerically.

The stationary waves of our problems are found through Newton's method, as now described. Consider the stationary set of equations (30)-(31), with $\partial_t = 0$. Following [30] we conclude that $\Theta = 0$ and

$$\Psi_\xi(\xi) = -F\mathrm{Y}_\xi(\xi) - \Omega\mathrm{Y}(\xi)\mathrm{Y}_\xi(\xi).$$

Therefore equations (30) and (31) are now written as

$$\begin{aligned}
&\mathrm{H}(\xi) = h(\mathrm{X}_b(\xi)),\\
&\mathrm{X}_b(\xi) = \xi - \mathcal{C}_0\left[\mathcal{F}^{-1}\left(\frac{\widehat{\mathrm{Y}}}{\cosh(kD)} - \frac{\widehat{H}}{\cosh^2(kD)}\right)\right] + \mathcal{T}[H],\\
&\mathrm{X}_\xi(\xi) = \frac{1}{D} - \mathcal{C}\left[\mathrm{Y}_\xi - \mathcal{F}^{-1}\left(\frac{\widehat{H}_\xi(k)}{\cosh(kD)}\right)\right],\\
&\Phi_\xi(\xi) = -\mathcal{C}\left[\left(\Psi_\xi(k) + \mathcal{F}^{-1}\left(\frac{(F-\Omega)\widehat{H}_\xi(k) + \frac{\Omega}{2}\widehat{\partial_\xi H^2}(k)}{\cosh(kD)}\right)\right)\right],\\
&\mathrm{Y} + \frac{1}{2J}(\Phi_\xi^2 - \Psi_\xi^2) + \frac{1}{J}(F + \Omega\mathrm{Y})\mathrm{X}_\xi\Phi_\xi - \Omega\Psi + P(\mathrm{X}) = 0.
\end{aligned} \tag{34}$$

The numerical stationary waves of the Euler equation are found on a domain $\xi \in [-L_E, L_E)$, with N_E uniformily spaced points with grid size $\Delta\xi = 2L_E/N_E$. On the grid points ξ_n, $n = 1, 2, ...N$, the steady

Bernoulli equation is written as

$$G_n(\mathrm{Y}_1, \mathrm{Y}_2, ..., \mathrm{Y}_N) := \mathrm{Y}_n + \frac{1}{2J}(\Phi^2_{\xi,n} - \Psi^2_{\xi,n}) + \frac{1}{J}(F + \Omega \mathrm{Y}_n)\mathrm{X}_{\xi,n}\Phi_{\xi,n} - \Omega\Psi_n + P_n. \tag{35}$$

We point out that all unknowns in equations (35) can be written in terms of Y, as was done in [3]. Fourier transforms and the operator $\mathcal{C}$ are approximated by the FFT on the uniform grid, and all derivatives are performed in Fourier space. The coefficient H_n is computed with the iterative scheme as before. The Jacobian for Newton's method is computed using

$$\frac{\partial G_n}{\partial \mathrm{Y}_l} = \frac{G_n(\mathrm{Y}_1, \mathrm{Y}_2, ..., \mathrm{Y}_l + \Delta\mathrm{Y}, ..., \mathrm{Y}_N) - G_n(\mathrm{Y}_1, \mathrm{Y}_2, ..., \mathrm{Y}_l, ..., \mathrm{Y}_N)}{\Delta\mathrm{Y}}.$$

The stopping criteria

$$\frac{\sum_{j=1}^{N} |G_n(\mathrm{Y}_1, \mathrm{Y}_2, ..., \mathrm{Y}_N)|}{J} < \delta,$$

was used for a give tolerance δ.

The stationary wave solutions are computed through Newton's method for topographic forcing only. The initial guess is $\mathrm{Y}_0(\xi) = 0$ and the bottom obstacle is given by $h(x) = (0.1/\pi^{1/2})e^{-0.1x^2}$. The stationary solution is then used as initial data for the time-dependent Euler solver. The discretization parameters are $\Delta\xi = 0.1$ and $N_E = 1024$. We will present one stationary irrotational wave and one stationary rotational wave. We will perturb both and observe their stability numerically.

First consider the irrotational case. For the supercritical regime $F \geq 1.3$, we found stationary waves of elevation, in resonance with the topography. Figure 10 displays the stationary wave for this case. It remains stationary when used as initial data for the time-dependent Euler solver. This wave agrees with the one generated from rest, after the transients have propagated away. In the regime $0 < F \leq 0.5$ stationary depression waves were found having oscillations on both sides, upstream and downstream.

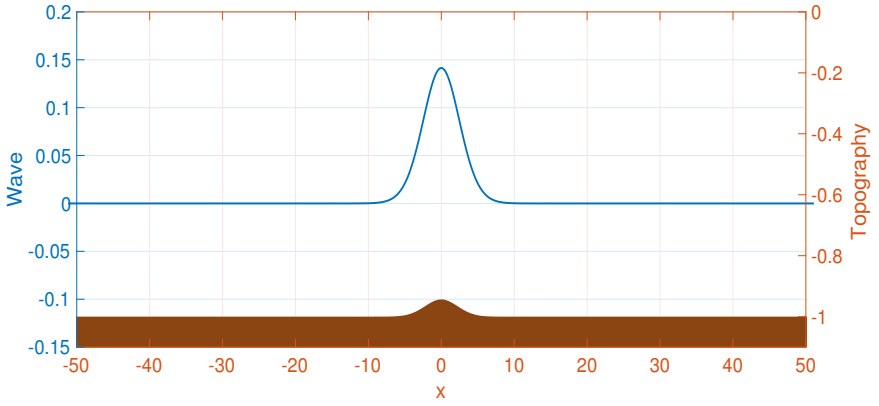

Figure 10: A stationary irrotational wave (in blue), found with Newton's method in the supercritical case ($F = 1.3$). The pulse-shaped wave is positioned above the topography (in brown), centered at the origin.

For rotational waves we present a supercritical case ($F = 1.25$) with constant vorticity $\omega = -1$. In this case Newton's method produces a periodic, oscillatory, stationary wave having a depression above the topography, as shown in figure 11. This profile remains stationary when used as initial data for the time-dependent Euler solver. Nevertheless it cannot be obtained from the initial state at rest.

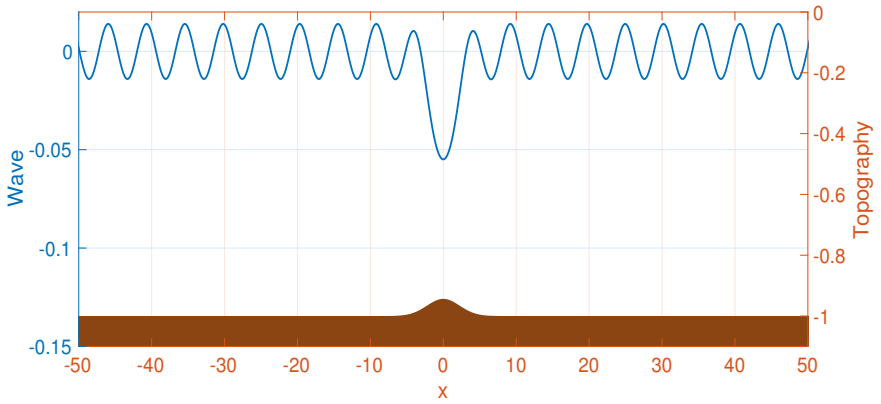

Figure 11: A stationary rotational wave (in blue; with $\omega = -1.0$), found with Newton's method in the supercritical case ($F = 1.25$). The wave is centered above the topography (in brown), located at the origin.

Denote the stationary wave profile by $\mathrm{Y}_S(\xi)$, which is used as initial condition in the corresponding Euler's equation solution $\mathrm{Y}(\xi, t)$. With

$$E_A \equiv \max_{0 \le t \le 1000} \max_{\xi} |\mathrm{Y}_S(\xi) - \mathrm{Y}(\xi, t)|,$$

we obtain a relative error of

$$E_R = \frac{E_A}{\max\limits_{\xi} |\mathrm{Y}_S(\xi)|} = \mathcal{O}(10^{-10}).$$

The stationary wave solution is indeed well approximated by the time-dependent Euler solver.

We next perturb these two stationary solutions. Denote by $\mathrm{Y}_S^0(\xi)$ the stationary solution, as above, which is now used as initial data. We perturb this initial wave profile through its amplitude, in the form $\alpha \mathrm{Y}_S^0(\xi)$, $\alpha > 0$. Chardard et al. [9] considered a similar scenario for studying perturbations to stationary solutions of the irrotational fKdV.

The stationary (irrotational) pulse-shaped wave is stable to perturbations, with both $\alpha > 1$ and $\alpha < 1$, always returning to its original amplitude. Of course there exists a critical value α_c such that wave breaking takes place for $\alpha > \alpha_c$. This is not the main theme of our study, so we exhibit a few cases. For $F = 1.3$ and $\Omega = 0$, as above, we found that $\alpha_c \approx 2.5$. For $1 < \alpha \le 2.4$ we observed that the excess mass propagated downstream with the wave returning to its equilibrium position. In figure 12 we have the initial profile for $\alpha = 1.5$. At time $t = 140$ we see that the stationary pulse has returned to its original stationary configuration, while a smaller pulse (having the excess mass) propagates downstream.

For $0 < \alpha < 1$, the stationary solutions were observed to be stable. In figure 13 we consider $\alpha = 0.5$. The smaller initial pulse recovers its original amplitude, gains mass and consequently generates a wave of depression downstream. We have not altered the parameters $F = 1.3$ and $\Omega = 0$.

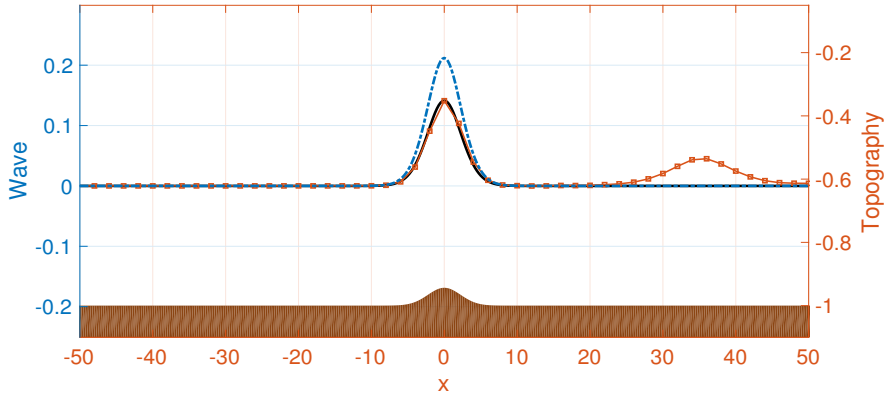

Figure 12: The stationary wave in figure 10 is perturbed by the factor $\alpha = 1.5$. The perturbed profile at $t = 0$ appears in a dashed (blue) line. Square markers (in red) indicate the numerical Euler solution at time $t = 140$ returning to the stationary (Newton method) profile given by the solid (black) line. The excess mass (in red square markers) is seen propagating downstream. The topography (in brown) is centered at the origin $x = 0$.

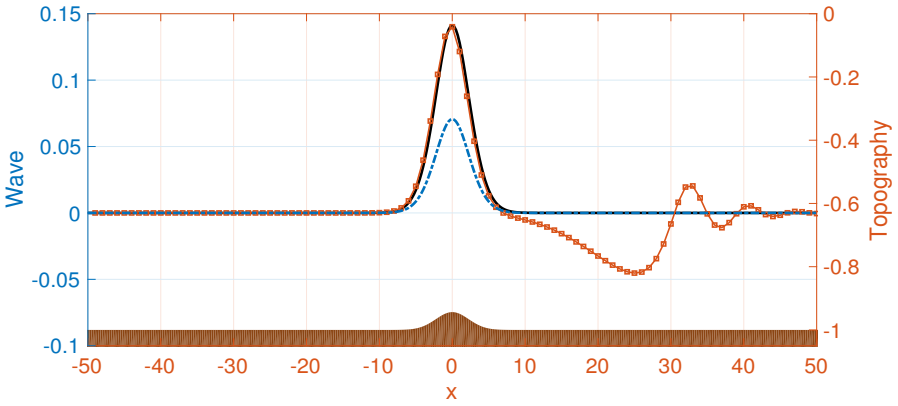

Figure 13: The stationary wave in figure 10 is reduced by a factor of $\alpha = 0.5$. The perturbed profile at $t = 0$ appears in a dashed (blue) line. Square markers (in red) indicate the numerical Euler solution at time $t = 70$ returning to the stationary (Newton method) profile given by the solid (black) line. The perturbed initial profile gained mass, from the underlying fluid body, and therefore a depression wave (in red square markers) propagates downstream. The topography (in brown) is centered at the origin $x = 0$.

Now we consider perturbing the stationary rotational wave. These are periodic oscillatory waves, as we saw above. When perturbed, these waves do not return to their original configuration. We increase its amplitude, the excess mass travels slowly around the periodic domain. As opposed to the pulse shaped stationary wave, the excess mass is always superimposed with the underlying stationary wave.

The perturbed wave profile, immediately above the topography, recovers its equilibrium position and it forces excess mass to propagate out in both directions. Stability in this case does not imply the return to the original configuration, as above, but a slow oscillatory behavior (in time) near the equilibrium position. Recall that the rotational regime has $F = 1.25$ and $\omega = -1$. We observed stability for $0 < \alpha < 1$. In figure 14 we display snapshots for the evolution of a perturbed initial profile with $\alpha = 0.5$.

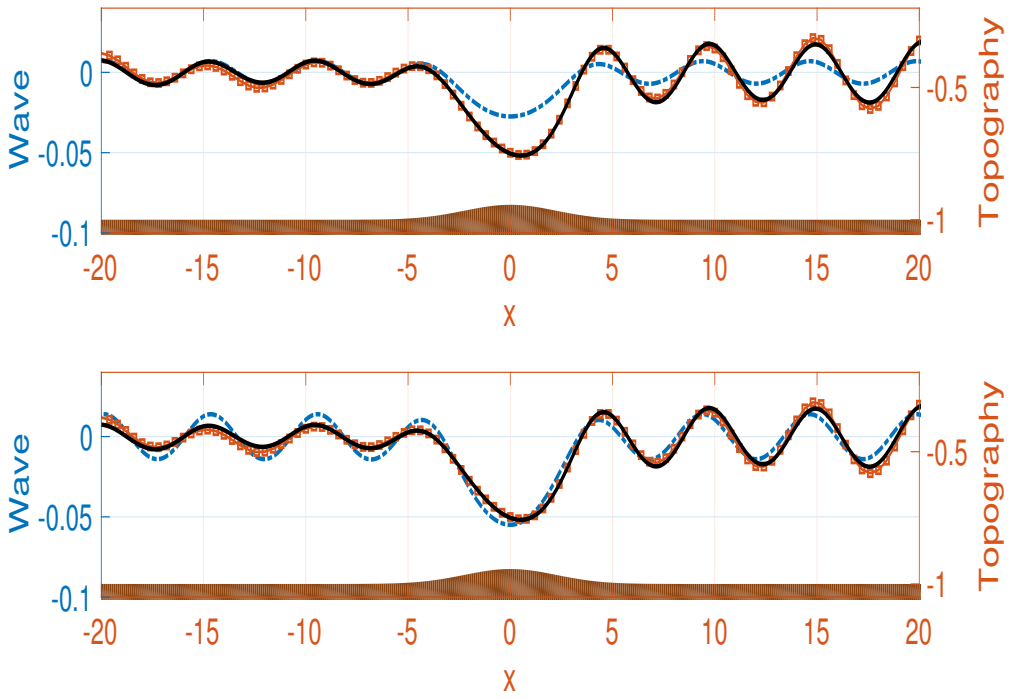

Figure 14: Supercritical rotational wave regime, with $F = 1.25$ and $\omega = -1$. At time $t = 0$, the stationary wave elevation is perturbed by a **reduction** factor of $\alpha = 0.5$. This is displayed in the top figure by the dashed-line. The computed Euler solutions are depicted at time $t = 80$ (red line with square markers) and at time $t = 140$ (solid line), and shown to depart from the perturbed stationary profile. At the bottom figure, the (same) computed Euler solutions (at $t = 80, 140$) have approached the unperturbed stationary profile (dashed line). Above the topography centered at $x = 0$, the stationary depression is fully recovered. The oscillations downstream also recover their amplitude, since excess mass, from the initial reduced depression, can more easily flow in this direction.

In figure 15 we present a case with $\alpha = 1.5$. Having excess mass upstream, away from the topography, the perturbed solution appears to adjust better than in the previous case. As time evolves, the perturbed solution slowly oscillates near the stationary profile, both upstream and downstream.

Boyd [41, 42] describes a permanent and steadily translating wave, satisfying requirements of a solitary wave except that it has an exponentially small oscillatory field along its sides. In analogy with having very small lateral wings, Boyd defines this wave as a "nanopteron". It is not clear that

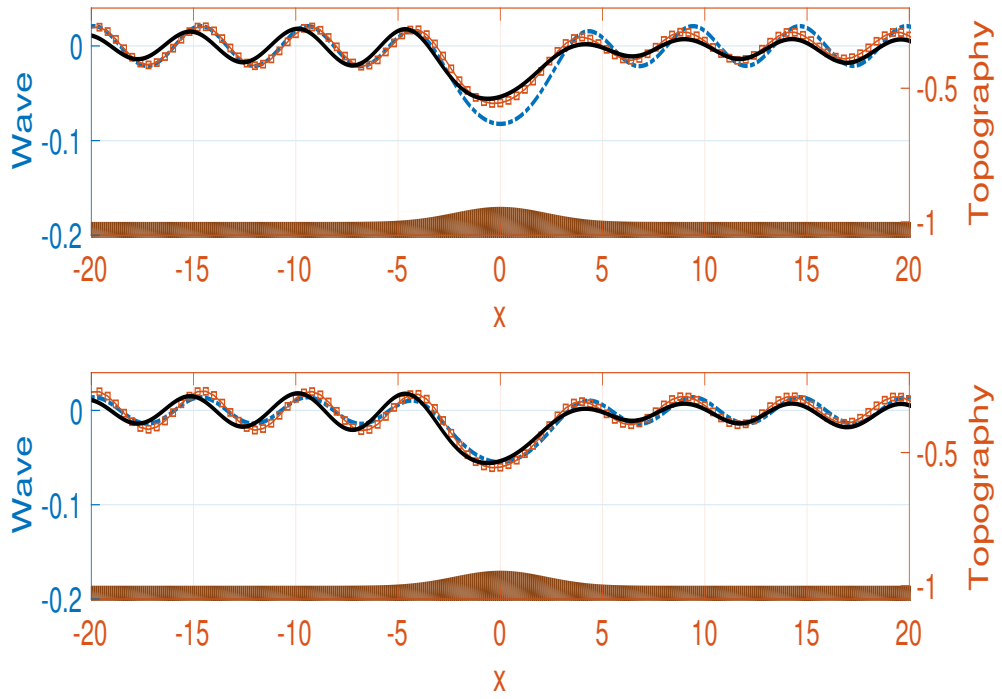

Figure 15: Supercritical rotational wave regime, with $F = 1.25$ and $\omega = -1$. At time $t = 0$, the stationary wave elevation is perturbed by a **dilation** factor of $\alpha = 1.5$. This is displayed in the top figure by the dashed-line. The computed Euler solutions are depicted at time $t = 140$ (red line with square markers) and at time $t = 250$ (solid line), and shown to depart from the perturbed stationary profile. At the bottom figure, the (same) computed Euler solutions (at $t = 140, 250$) have approached the unperturbed stationary solution (dashed line). The initial depression recedes (from -0.08 to -0.06), above the topography centered at $x = 0$, and the lateral oscillations adjust their amplitudes regarding the stationary solution, depicted by a dashed line in the bottom figure.

our stationary waves are related to "nanopterons", which in our case are displaying finite amplitude oscillations. Having in mind the interested reader, we refer to Boyd's work as well as an article by Akylas and Grimshaw [43], where asymptotics above all orders is used to obtain an internal solitary wave with exponentially small oscillatory tails.

6 Conclusion

A forced Korteweg-de Vries equation (fKdV) was deduced incorporating the effect of a sheared-current (of constant vorticity) while being forced by a bottom topography and a pressure distribution along the free surface. Rotational waves are spontaneously generated by the forcing and compared to those

generated by the more complete Euler equations. The numerical model for the Euler equations considers the harmonic component of the velocity field. Using a conformal mapping it is solved on a flat strip, which permits Fourier integral representation for all the objects of interest. Numerical solutions for both models are compared as the amplitude of the topography gradually increases. As the fKdV regime ceases to be satisfied we observe the onset of wave breaking with the Euler equations.

Of particular interest, we show that vorticity shifts the critical Froude number enabling a change of regime, say from critical to supercritical, or supercritical to subcritical. A recent theoretical study by Wheeler [39] shows how the Froude number may be suitably redefined in the presence of vorticity. Wheeler's stationary wave analysis considers solitary waves through the Dubreil-Jacotin formulation.

Through Newton's method, we obtained novel stationary waves. The stationary, rotational wave cannot be obtained starting from rest, as in the previous cases. Nevertheless it satisfies the evolution scheme and remains invariant in time. Numerically we test the stability of the stationary waves. They are stable to amplitude perturbations.

7 Acknowledgements

We thank both referees for their valuable comments and suggestions.

The work of M.F. was supported in part by CNPq-Science without Borders under (PDE) 200920/2014-6 and by CNPq-Cotas do Programa de Pós-Graduação (GM/GD) 140773/2014-2. The work of P.A.M. was supported in part by a Royal Society Wolfson award and a CNPq-Science without Borders award no. 402178/2012-2. The work of A.N. was supported in part by CNPq under (PQ-1B) 301949/2007-7 and FAPERJ Cientistas do Nosso Estado project no. 102.917/2011.

A Numerical resolution study

In this appendix we present results from a resolution study with the Euler equations. In order to compute the relative error, we use as our reference solution the wave elevation ζ computed on our finest grid, with $\Delta\xi = 0.025$ in the canonical domain. The results presented in this article used $\Delta\xi = 0.1$.

Results for the irrotational regime, in the critical Froude number case, are displayed in table 1. The relative error (in ℓ_2) decays as the mesh size is continuously reduced by a factor of 2. In figure 16 we see that the well developed wave profile is accurately captured by all discretizations. In figure 17 we zoom into two regions of the wave elevation. A detailed view is presented, one from the wavefront propagating upstream (near $x = -12.8$) and another along the oscillatory wave train propagating downstream (near $x = 41$).

We present a similar table and wave profile for the rotational regime, in the respective critical ($F_\omega = 1.28$) Froude number case. In table 2 we have the decay of the relative error, as the mesh size decreases. In figure 18 we see that the well developed wave profile is accurately captured by all discretisations. In figure 19 we zoom into a region of the wave elevation and a detailed view is presented.

References

[1] A.F. TELES DA SILVA, and D.H. PEREGRINE, Steep, steady surface waves on water of finite depth with constant vorticity, *J. Fluid Mech.*, 195:281-302 (1988).

ω	F	$\Delta\xi$	$\|\|\zeta_{\Delta\xi} - \zeta\|\|_2/\|\|\zeta\|\|_2$
0	1	0.8	0.300088370687047
0	1	0.4	$2.897204128606614 \times 10^{-5}$
0	1	0.2	$4.366197411567467 \times 10^{-7}$
0	1	0.1	$8.905938494107258 \times 10^{-8}$
0	1	0.05	$1.555076271898401 \times 10^{-15}$

Table 1: Euler solutions in the irrotational regime, in the critical ($F = 1$) Froude number case. The reference solution ζ is for the finest grid with $\Delta\xi = 0.025$.

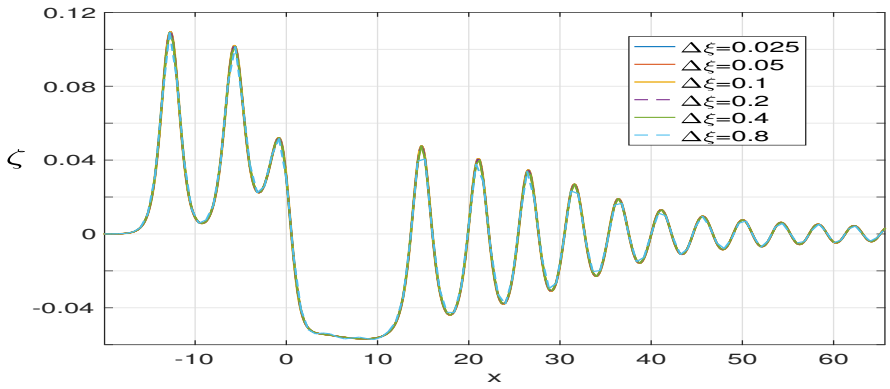

Figure 16: Critical $F = 1$ regime, with the Euler equations. A fully developed irrotational wave profile for different mesh sizes. The topography is centered at the origin $x = 0$.

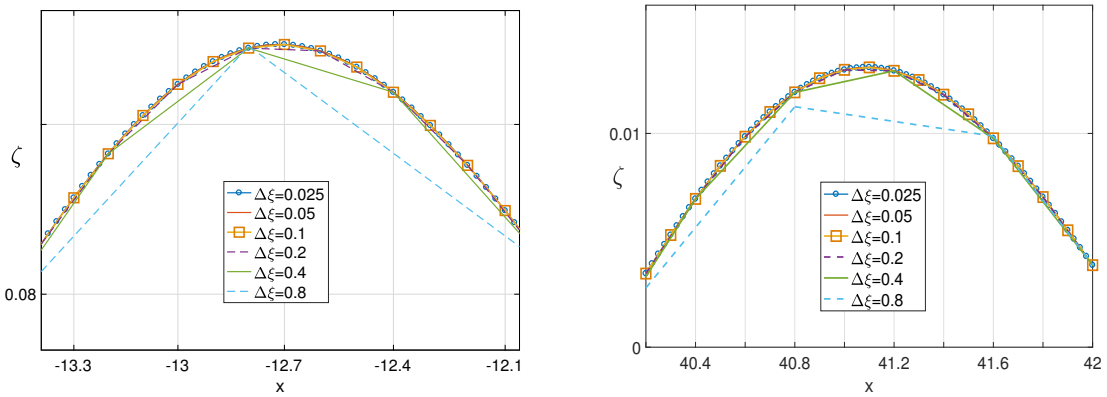

Figure 17: Details of figure 16. Left: near the wavefront propagating upstream. Right: along the oscillatory wave train propagating downstream.

ω	F_ω	$\Delta\xi$	$\|\|\zeta_{\Delta\xi} - \zeta\|\|_2/\|\|\zeta\|\|_2$
0.5	1.28	0.8	$1.4880722647593 \times 10^{-2}$
0.5	1.28	0.4	$2.303287095887669 \times 10^{-7}$
0.5	1.28	0.2	$1.619462262180957 \times 10^{-8}$
0.5	1.28	0.1	$1.619462210778736 \times 10^{-8}$
0.5	1.28	0.05	$1.619462206849179 \times 10^{-8}$

Table 2: Euler solutions in the rotational regime, in the critical ($F_\omega = 1.28$) Froude number case. The reference solution ζ is for the finest grid with $\Delta\xi = 0.025$.

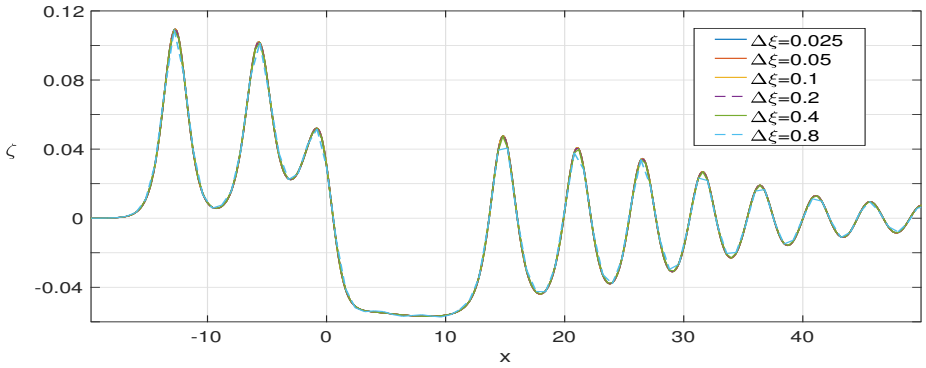

Figure 18: Critical $F_\omega = 1.28$ regime, with the Euler equations. A fully developed rotational wave profile for different mesh sizes. The topography is centered at the origin $x = 0$.

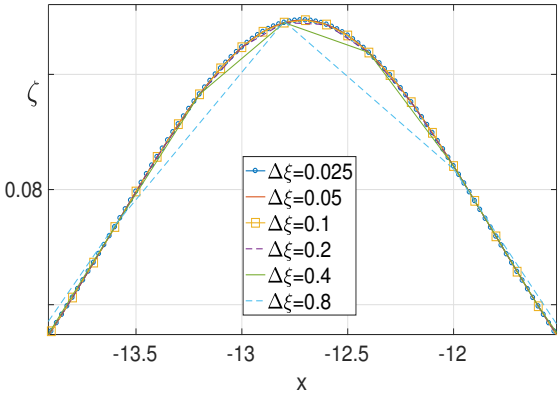

Figure 19: Detail of figure 18.

[2] V. VASAN and K. OLIVERAS, Pressure beneath a traveling wave with vorticity constant, *DSDC-A*, 34: 3219-3239, (2014).

[3] R. RIBEIRO-JR, P.A.MILEWSKI and A. NACHBIN Flow structure beneath rotational water waves, *J. Fluid. Mech.*, (2017).

[4] A. CONSTANTIN, Nonlinear water waves: introduction and overview. *Phil. Trans. R. Soc. A*, 376: 20170310, (2018).

[5] A. CONSTANTIN, W. STRAUSS and E. VARVARUCA, Global bifurcation of steady gravity water waves with critical layers. *Acta Math.*, 217:195-262, (2016).

[6] A.L. DYACHENKO, V.E. ZAKHAROV and E.A. KUZNETSOV, Nonlinear dynamics of the free surface of an ideal fluid, *Plasma Phys. Rep.*, 22:916-928, (1996).

[7] A. NACHBIN, A terrain-following boussinesq system, *SIAM J. APPL, MATH.*, 63:905-922 (2003).

[8] B. J. BINDER F. DIAS. and J. M, VANDEN-BROECK, Forced solitary waves and fronts past submerged obstacles, *Chaos 15.*, 15, 037106, (2005).

[9] F. CHARDARD, F. DIAS, H.Y. NGUYEN and J. M, VANDEN-BROECK, Stability of some stationary solutions to the forced KdV equation with one or two bumps, *Journal of Engineering Mathematics.*, 70 pp. 175-189, (2011).

[10] G. B. WHITHAM , Linear and Nonlinear Waves, *Wiley.*, (1974).

[11] J. ASAVANANT, M. MALEEWONG and J. CHOI, Computation of free-surface flows due to pressure distribution, *Korean Math. Soc.*, 16, 137-152, (2001).

[12] J. M. VANDEN-BROECK, Steep solitary waves in water of finite depth with constant vorticity, *J. Fluid Mech.*, 274, 339-348, (1994).

[13] J. M. VANDEN-BROECK and E. TUCK, Waveless free-surface pressure distributions, *J. Ship Res.*, 29, 151-158, (1985).

[14] L. J. PRATT, On nonlinear flow with multiple obstructions, *J .Atmos. Sci.*, 41:1214-1225, (1984).

[15] L. N. TREFETHEN, Spectral Methods in MATLAB, *Philadelphia: SIAM.*, (2001).

[16] M. D. ALBALWI, T. R. MARCHANT and N. F. SMYTH, Higher-order modulation theory for resonant flow over topography, *Physics of Fluids.*, 29, 077-101, (2017).

[17] N. C. FREEMAN and R. S. JOHNSON, Shallow water waves on shear flows, *J. Fluid Mech.*, 42, 401-409, (1970).

[18] P. MILEWSKI, J. M, VANDEN-BROECK and Z. WANG, Dynamics of steep two-dimensional gravity-capillary solitary waves, *J. Fluid Mech.*, 664:466-477, (2010).

[19] P. MILEWSKI and E. G, TABAK, A pseudo-spectral algorithm for the solution of nonlinear wave equations, *SIAM J. Sci. Comp.*, 1102-1114, (1999).

[20] R. CAMASSA and T. Y. WU, Stability of forced steady solitary waves, *Philos. Trans. R. Soc. Lond.*, A337:429-466, (1991).

[21] R. CAMASSA and T. Y. WU, Stability of some stationary solutions for the forced KdV equation, *Physica.*, D51:295-307, (1991).

[22] R. GRIMSHAW, and M. MALEEWONG, Stability of steady gravity waves generated by a moving localized pressure disturbance in water of finite depth, *Phys. Fluids.*, 25, 076605, (2013).

[23] R. H. GRIMSHAW and N. SMYTH, Resonant flow of a stratified fluid over topography, *J. Fluid Mech.*, 169:429-464, (1986).

[24] S. LEE, Generation of long water waves by moving disturbances, *Ph.D. thesis, California Institute of Technology, Pasadena, CA.*, (1985).

[25] C. VIOTTI, D. DUTYKH and F. DIAS, The conformal-mapping method for surface gravity wave in the presence of variable bathymetry and mean current, *IUTAM Proc.*, 11:110-118, (2014).

[26] C. VIOTTI and F. DIAS, Extreme waves induced by strong depth transitions: Fully nonlinear results, *Phys. Flu.*, 26:051705, (2014).

[27] T.R. AKYLAS, On the excitation of long nonlinear water waves by a moving pressure distribution, *J Fluid. Mech.*, 141:455-466, (1984).

[28] T. Y. WU, Generation of upstream advancing solitons by moving disturbances, *J. Fluid. Mech.*, 184:75-99, (1987).

[29] T. Y. WU and D. M. WU, In Proc. 14th Symp. on Naval Hydrodynamics, *4th Symp. on Naval Hydrodynamics, Washington, D.C. National Academy of Sciences.*, pp. 103-125 (1982).

[30] W. CHOI, Nonlinear surface waves interacting with a linear shear current, *IMACS.*, (2009).

[31] W. CHOI and R. CAMASSA, Exact evolution equations for surface waves, *J. Eng. Mech.*, 125:756-760, (1999).

[32] B. WANG and L.G. REDEKOPP, Long internal waves in shear flows: topographic resonance and wave-induced global instability, *Dyn. Atmos. Oceans*, 33:263-302, (2001).

[33] P.G. BAINES, Topographic effects in stratified flows, *Cambridge University Press*, (1995).

[34] R. H. GRIMSHAW and Z. YI, Resonant generation of finite-amplitude waves by the flow of a uniformly stratified fluid over topography , *J. Fluid Mech.*, 229:603-628, (1991).

[35] K.R. HELFRICH and W.K. MELVILLE, Long nonlinear internal waves, *Annu. Rev. Fluid Mech.*, 38:395-425, (2006).

[36] K.G. LAMB, Internal wave breaking dissipation mechanism on the continental slope/shelf, *Annu. Rev. Fluid Mech.*, 46:231-254, (2014).

[37] N. SOONTIENS, C. SUBICH and M. STASTNA, Numerical simulation of supercritical trapped internal waves over topography, *Phys. Fluids*, 22:116605, (2010).

[38] M. STASTNA and W.R. PELTIER, On the resonant generation of large-amplitude internal solitary-like waves, *J. Fluid Mech.*, 543:267-292, (2005).

[39] M. H. WHEELER, The Froude number for solitary water waves with vorticity, *J. Fluid Mech.*, 768:91-112, (2015).

[40] R.S. JOHNSON, A Modern Introduction to the Mathematical Theory of Water Waves, *Cambridge University Press*, (1997).

[41] J. BOYD, New directions in solitons and nonlinear periodic waves, 2:82 *Advances in Applied Mechanics*, Ed. J.W. Hutchinson and T.Y. Wu, *Academic Press*, (1990).

[42] J. BOYD, Weakly non-local solitons for capillary-gravity waves: fifth-degree Korteweg-de-Vries equation *Phys. D*, 48:129-146, (1990).

[43] T.R. AKYLAS and R. GRIMSHAW, Solitary internal waves with oscillatory tails, *J. Fluid Mech.*, 242:279-298, (1992).

Universidade Federal Rural de Pernambuco
University of Bath
Instituto Nacional de Matemática Pura e Aplicada